The Bow and Arrow Mesoscale Convective Structure

KELLY M. KEENE

Department of Atmospheric Sciences, Texas A&M University, College Station, Texas, and National Center for Atmospheric Research, Boulder, Colorado*

RUSS S. SCHUMACHER

Department of Atmospheric Sciences, Texas A&M University, College Station, Texas, and Department of Atmospheric Science, Colorado State University, Fort Collins, Colorado

(Manuscript received 15 June 2012, in final form 5 October 2012)

ABSTRACT

The accurate prediction of warm-season convective systems and the heavy rainfall and severe weather associated with them remains a challenge for numerical weather prediction models. This study looks at a circumstance in which quasi-stationary convection forms perpendicular to, and above the cold-pool behind strong bow echoes. The authors refer to this phenomenon as a ''bow and arrow'' because on radar imagery the two convective lines resemble an archer's bow and arrow. The ''arrow'' can produce heavy rainfall and severe weather, extending over hundreds of kilometers. These events are challenging to forecast because they require an accurate forecast of earlier convection and the effects of that convection on the environment. In this study, basic characteristics of 14 events are documented, and observations of 4 events are presented to identify common environmental conditions prior to the development of the back-building convection. Simulations of three cases using the Weather Research and Forecasting Model (WRF) are analyzed in an attempt to understand the mechanisms responsible for initiating and maintaining the convective line. In each case, strong southwesterly flow (inducing warm air advection and gradual isentropic lifting), in addition to directional and speed convergence into the convective arrow appear to contribute to initiation of convection. The linear orientation of the arrow may be associated with a combination of increased wind speeds and horizontal shear in the arrow region. When these ingredients are combined with thermodynamic instability, there appears to be a greater possibility of formation and maintenance of a convective arrow behind a bow echo.

1. Introduction

Bow echoes are mesoconvective structures that can be long lived and cover distances of 20–200 km (Glickman 2000). They consist of a bow-shaped segment of smaller reflectivity echoes. These systems are known for producing long swaths of damaging winds, as well as heavy precipitation and occasionally tornadoes. They usually initiate as either weakly organized cells, squall lines, or supercells, and are most commonly found in the central United States (Klimowski et al. 2004).

As outlined by Fujita (1978; Fig. 1), these systems typically begin with a strong, large single cell of convection that is either completely isolated or is part of a larger squall line. Additional cells develop adjacent to this cell, forming a bow shape of segmented cells. This coincides with strengthening surface winds, where the strongest winds are found at the apex of the bow. When the bow echo reaches its greatest intensity, it forms a cyclonic circulation on one end, and an anticyclonic circulation on the other end. Eventually the system will evolve into a comma shape, only maintaining the cyclonic head on the left flank (Fujita 1978).

Behind and within the area of strongest convection in a bow echo, evaporative cooling occurs as a result of dry midtropospheric entrainment and precipitating downdrafts

* The National Center for Atmospheric Research is sponsored by the National Science Foundation.

Corresponding author address: Kelly Keene, National Center for Atmospheric Research, P.O. Box 3000, Boulder, CO 80307-3000.
E-mail: kkeene@ucar.edu

DOI: 10.1175/MWR-D-12-00172.1

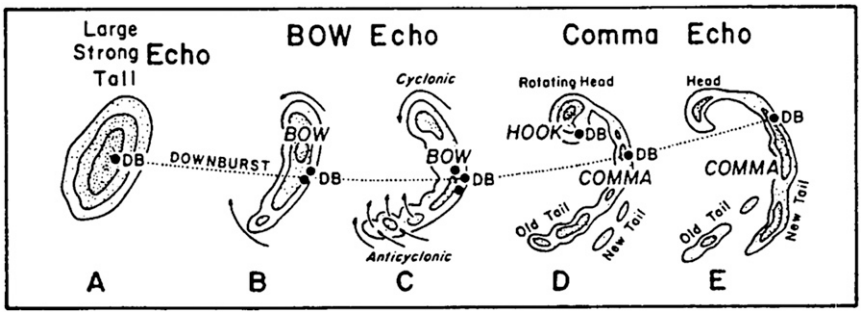

FIG. 1. A typical morphology of radar echoes associated with bow echoes that produce strong and extensive downbursts, labeled DB on the figure (Adapted from Fujita 1978).

(Goff 1976) and forms a cold pool. This dense cool air spreads out in a shallow layer along the surface behind the bow echo and forms an outflow boundary along its periphery. Because this boundary converges with warmer, less-dense air it often acts as a density current, creating lifting at its edges. Corfidi (2003) shows that it is common for additional convective lines to form along the outflow boundary. The current study investigates what we term the ''bow and arrow''—a circumstance in which back-building convection forms in an orientation quasi-perpendicular to, and elevated above the cold pool behind strong bow echoes (i.e., not along the outflow boundary). Nine examples of this phenomenon are shown in Fig. 2, using composite radar imagery. Each image shows a bow echo with an arrow following. It is evident that the orientation of the arrow can vary between cases. It is not always centered behind the bow, and is not always perfectly perpendicular to the bow; however, in each case, it is located behind the bow echo, elevated above the cold pool, and is quasi-linear.

Past modeling studies (e.g., Weisman and Klemp 1986; Rotunno et al. 1988; Weisman et al. 1988) have determined conditions favorable for the upscale development of convective cells into lines. Lifting at the leading edge of the spreading surface cold pool causes the development of deep convection in a bow-shaped arc. Convective cells are more likely to form a bow-shaped arc when there is large convective available potential energy (CAPE) of at least 2000 J kg^{-1} and strong low-level vertical wind shear of at least 20 m s^{-1} over the lowest 5 km above ground level. The bow shape is directly due to the regeneration of convective cells along the downshear segment of the spreading cold pool (Weisman 1993). The bow is oriented perpendicular to the vertical wind shear vector. Mechanisms governing the orientation and sustenance of the arrow segment of the mesoscale convective system (MCS) are less well understood, and the idealized simulations used in these past studies did not produce arrows (M. Weisman 2012, personal communication). LeMone et al. (1998) and Johnson et al. (2005) showed examples of convective bands oriented behind and perpendicular to a leading line, but it is unclear whether the processes leading to those lines in the tropics are similar to those causing the arrows in midlatitudes.

One of the consequences of the bow and arrow is its threat for extreme rainfall that can lead to flash flooding. The arrow is typically quasi-stationary, wherein several convective cells reach maturity and produce their heaviest rainfall over the same area (e.g., Chappell 1986; Doswell et al. 1996; Schumacher and Johnson 2005). A combination of precipitation resulting from the bow echo and additional rainfall associated with the quasi-stationary (or back building) convective arrow can result in a large amount of precipitation in a particular area. Additionally, these systems are capable of producing potentially damaging severe winds and hail.

It is important to consider the environmental conditions necessary for producing MCSs and bow echoes to determine the ingredients needed for a bow and arrow, as well. It is expected that many of the conditions are similar to those associated with bow echoes in general, but there may be key additional processes that help discriminate environments most favorable for the production of the trailing arrow. Identifying common environmental conditions prior to development of back-building convection—in addition to understanding the mechanisms responsible for initiating and maintaining the convective line—could result in useful guidance for operational forecasters.

In this paper, we analyze observations to determine environmental conditions prior to the development of the bow echo. A combination of surface analysis, with an overlay of radar composites, and upper-air observations are reviewed. This provides a broad view of the synoptic-scale setting prior to, and during, the phenomenon.

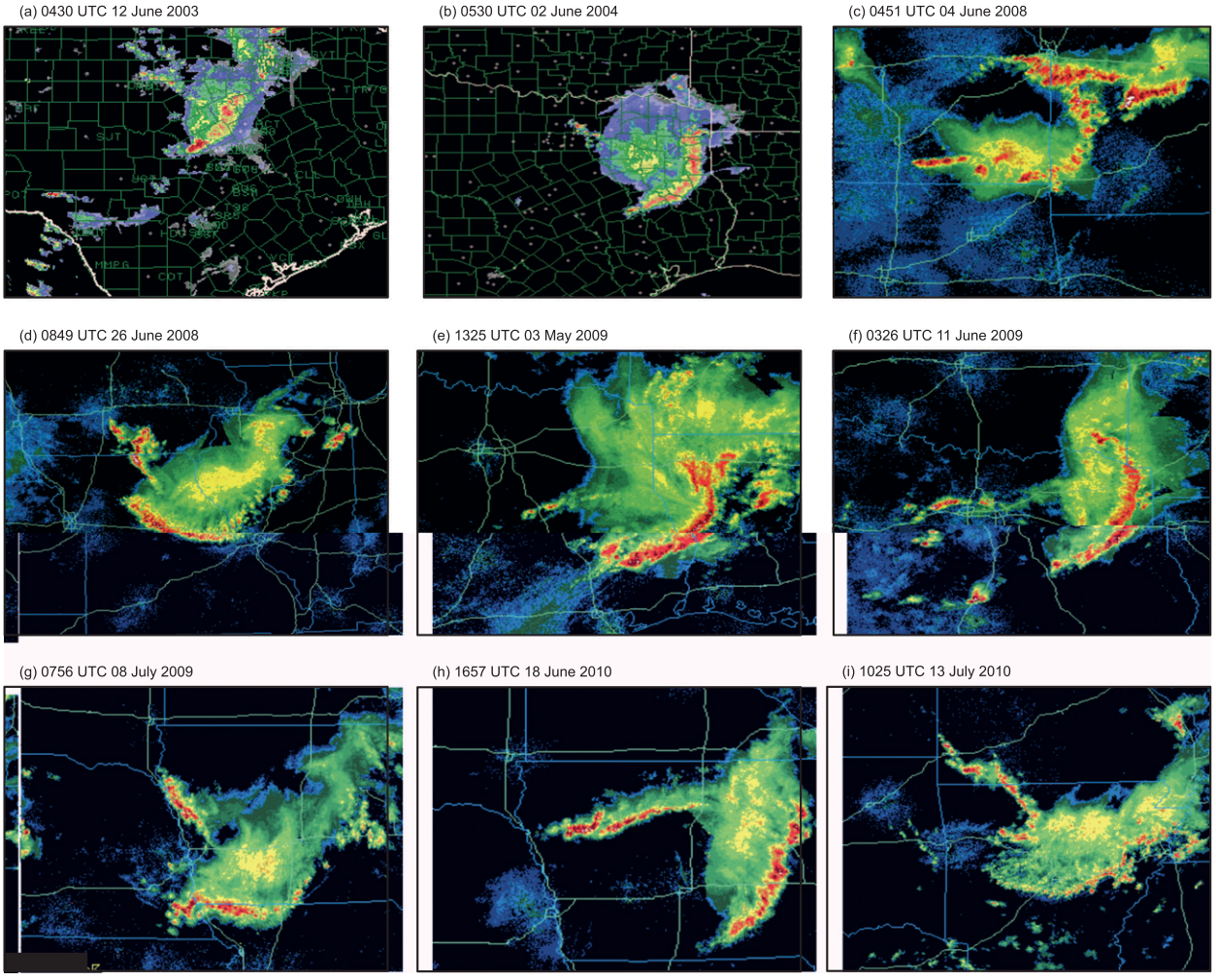

FIG. 2. Composite radar reflectivity for (a) 0430 UTC 12 Jun 2003, (b) 0530 UTC 2 Jun 2004, (c) 0451 UTC 4 Jun 2008, (d) 0849 UTC 26 Jun 2008, (e) 1325 UTC 3 May 2009, (f) 0326 UTC 11 Jun 2009, (g) 0756 UTC 8 Jul 2009, (h) 1657 UTC 18 Jun 2010, and (i) 1025 UTC 13 Jul 2010, showing the varying structure of the bow and arrow, with a leading convective bow echo, followed by elevated convection (the arrow), quasi perpendicular to the leading line, and elevated above the cold pool behind the bow echo.

To obtain a further understanding of mesoscale aspects of the bow and arrow structure, the cases are reproduced through model simulation. Several different combinations of model physical parameterizations and initial conditions are used in an attempt to recreate the bow and arrow as precisely as possible. Successful simulations are examined in more detail to reach a conclusion about the processes responsible for such an event.

Section 2 will provide the data and methods used to carry out analysis of these events. Section 3 will give a discussion of the synoptic-scale environment prior to, and during the events, in addition to impact verification. Section 4 will break down the three cases and discuss the analysis of model output. Conclusions and anticipated future work will be discussed in section 5.

2. Data and methods

a. Selection of cases

The first identification of the bow and arrow phenomenon was through previous work regarding extreme rainfall produced by convective systems (Schumacher and Johnson 2006), and other cases were identified through manual inspection of radar reflectivity observations. Although thorough, searching through daily radar archives to find additional cases is time consuming; therefore, utilizing Hovmöller time–distance diagrams of estimated rainfall rate (Carbone et al. 2002) is a more efficient method for locating certain patterns that may be indicative of a bow and arrow. Figure 3 shows an example of one such diagram from 5 July 2003 (a day on which a bow and arrow occurs), where the area of

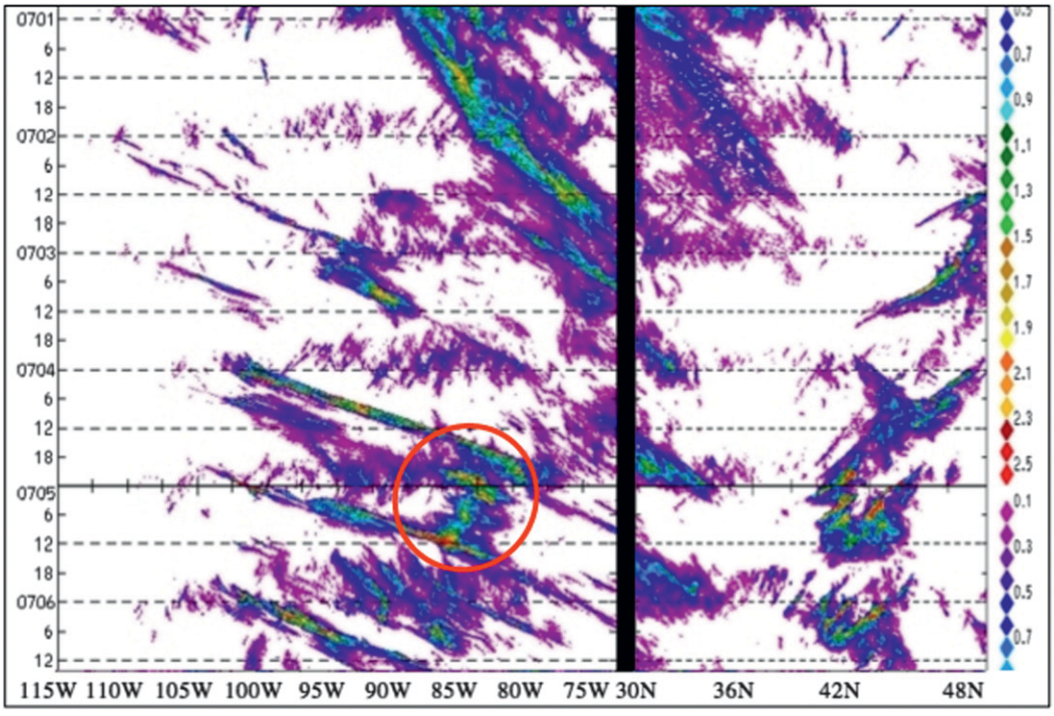

FIG. 3. Hovmöller diagram representing time–distance data of estimated rainfall from 1– 6 Jul 2003. The left side of the *X* axis represents evenly spaced longitudinal points across the United States (75°–115°W), while the right side of the *X* axis shows points of latitude across the United States (30°– 48°N). The *Y* axis represents days of the month, increasing toward the bottom, with tick marks every 6 h (0000–1800 UTC). The red circle indicates the area of interest, as described in the text. (From NCAR's Mesoscale and Microscale Meteorology Division precipitation episodes website http://www.mmm.ucar.edu/episodes/Hovmoller/index.html.)

interest is circled. This particular pattern portrays precipitation that occurs over two consecutive days, generally moving from west to east as time progresses (shown by the two diagonal streaks, extending longitudinally over time). It also shows quasi-stationary precipitation over one area (the area of increased precipitation that connects the two diagonal streaks). This potentially portrays a slow-moving MCS or other heavy precipitating event. Once the above-mentioned pattern is recognized on a particular day, archived radar animations are observed to visually determine whether a bow and arrow actually occurs. Hovmöller diagrams are examined for a course of 12 warm seasons (1996–2007) to identify suitable cases. Several other cases are identified in radar imagery in real time, and others were previously identified among the cases analyzed by Schumacher and Johnson (2005, 2006).

A total of 14 cases occurring from August 1999–September 2010 are identified using the methods described above (Table 1). All of the cases occur during the warm season (May–September), and in the Great Plains or Midwest regions of the United States (Fig. 4). This is the area and time period that is commonly associated with the occurrence of MCSs, as well as bow echoes (Augustine and Caracena 1994). In several of the cases, the bow-and-arrow process occurred multiple times.

The duration of the arrow ranged from 1.5 to 6.5 h, with an average of 3.5 h. The time difference between the passage of the bow echo in one location, and the formation of the arrow in that location, for all cases, is between 1 and 5 h, with an average of 2 h. Several of the arrows were associated with severe hail (0.75 in. prior to 2010, 1 in. after), severe winds (gusts in excess of 50 kt, 1 kt = 0.5144 m s^{-1}), or flash flooding, and more than one of these hazards were reported in a few cases. Although only 14 cases are used in this study, it is likely that other events occurred during this time period, but were not identified by our selection methods. Nonetheless, this represents a reasonable sample of events to study.

Observations of four cases are examined in more detail, and three of those cases are numerically simulated to help determine the more detailed environmental conditions that may favor the occurrence of the bow and arrow MCS. Of several cases simulated, these three cases are the only ones that are able to be

TABLE 1. Dates of bow and arrow events with their location, time of day, duration, time between the passage of the bow echo, the appearance of the first convective cells of the arrow, and the number of severe storm reports (where H represents hail, W represents severe wind, and F represents flash flood reports). Storm reports were obtained from the Storm Prediction Center (NOAA 2012a), and flash flood reports were obtained from the Iowa State University (2012). Only those reports directly caused by the arrow are shown. Except for the 5 Jul 2003 event, a consistent record of flash flood reports from prior to 2006 was unavailable; ''NAF'' indicates flood reports not available. Times are in UTC, and are determined based on the time that the first convective cells in the arrow are observed. Some of the cases have multiple times listed because there were multiple arrows on that day. The duration is the length of time (in h) that the arrow was present in radar reflectivity (not the duration of the MCS as a whole).

Date	Location	Time (UTC)	Duration (h)	Time between bow echo and formation of arrow (h)	No. of storm reports
30 Aug 1999	South Dakota	0300, 0530	1.5, 3	1.5, 1.5	None/NAF
12 Jun 2003	Texas	0230	5	1	None/NAF
5 Jul 2003	Indiana–Illinois	0115, 0515	3, 2	4, 1.5	1H/3W/15F
2 Jun 2004	Texas	0400	5	1.5	None/NAF
18 Jun 2006	Texas	0430	5	2	2H
4 Jun 2008	Kansas	0315	3	1	2H
26 Jun 2008	Iowa–Missouri	0645, 1100	3.5, 2	2, 1.5	4H/1F
3 May 2009	Texas–Louisiana	1225	2	2	None
8 May 2009	Missouri–Arkansas	1530	4	2	2F
11 Jun 2009	Texas	0000	4	2.5	None
8 Jul 2009	Iowa–Nebraska	0600	3	2.5	None
18 Jun 2010	Iowa	1430	5	2.5	11H/3W
13 Jul 2010	Missouri–Arkansas	0830	2	5	2F
15 Sep 2010	Nebraska–Kansas–Missouri	0300, 1130, 1600	6.5, 2, 4.5	1.5, 2.5, 1.5	1F

reproduced by numerical model simulation, and given the similarities of the output analysis (discussed later), they are believed to be a reasonable representation of the total population of cases. The cases occurred on 18 June 2006, 8 May 2009, and 15 September 2010, which will hereafter be referred to as case 1, case 2, and case 3, respectively.

b. Model simulations

Table 2 shows details regarding the model configuration for the three simulated cases. The initial and boundary conditions for all three cases come from the 6-hourly North American Mesoscale Model (NAM) 212 grid (40 km) output. The model used is the Advanced Research Weather Research and Forecasting Model (ARW-WRF) (Skamarock and Klemp 2008). The output for cases 1 and 2 comes from previous simulations from the National Center for Atmospheric Research's (NCAR's) real-time forecast project (Weisman et al. 2008). These both use one large high-resolution domain, while case 3 is run with a large coarse mesh domain that includes two nested grids (Fig. 5). For cases 2 and 3, a positive definite moisture advection scheme is used (Skamarock and Weisman 2009). This scheme significantly reduces positive bias for surface precipitation forecasts, especially in high precipitation cases (this scheme was not available at the time case 1 was simulated). A simulation is considered successful if it includes both a bow echo and a trailing convective arrow in simulated radar reflectivity imagery.

3. Observational analysis

Observations are analyzed to determine environmental conditions prior to, and during each event. Operational upper-air observations and surface analyses [(National Oceanic and Atmospheric Administration) NOAA 2012b] are examined, and although useful for assessment of synoptic conditions, they are too sparse to

FIG. 4. Distribution of bow and arrow events from 1999–2010. The bullets indicate location of the convective arrow in each case.

TABLE 2. Configuration of ARW-WRF simulations for cases 1, 2, and 3. This table provides information regarding the date of each case, the large-scale model from which the input data came, horizontal grid spacing for the domains, microphysical schemes, planetary boundary layer schemes, and cumulus parameterization schemes used, as well as the version of the model that was used. Details of these parameterizations can be found in Skamarock et al. (2008).

Date	Input data	Horizontal grid spacing (km)	Microphysics	PBL scheme	Cumulus parameterization	ARW-WRF version
18 Jun 2006	NAM	4	Hong and Lim (2006)	Janjic (1994)	None	2.1.2
8 May 2009	NAM	3	Thompson et al. (2008)	Janjic (1994)	None	3.1
15 Sep 2010	NAM	27, 9, 3	Hong and Lim (2006)	Hong et al. (2006)	Kain (2004), outer 2 domains	3.2

determine mesoscale details important for bow and arrow formation. The Barnes objective analysis method (Koch et al. 1983) is used for creating mesoscale analyses of sea level pressure, temperature, and surface station observations, which are overlaid with radar reflectivity composites. The four cases used for observational analysis include the three cases used in model simulation, as well as a case from 5 July 2003. The July 2003 case was not satisfactorily reproduced through model simulation, as was also noted in previous studies (e.g., Metz and Bosart 2010; Wheatley and Stensrud 2010), which is perhaps indicative of the low predictability of this phenomenon. However, it is used for observational discussion because it is an exemplary illustration of the bow and arrow phenomenon.

a. An archetypal bow and arrow

On the late afternoon of 4 July 2003, and into the early morning hours of 5 July, convection that began over northwest Illinois moved eastward, organizing into a leading-line, trailing stratiform (e.g., Parker and Johnson 2000) MCS. The leading line of convection evolved into a bow echo over northeastern Indiana around 0000 UTC (Fig. 6a). Around 0130 UTC, as the bow moved toward the southeast and into western Ohio, convective cells appeared in northwest Indiana (Fig. 6b). By 0200 UTC, an organized line of convective cells formed an arrow behind the initial leading convective line (Fig. 6c). By 0400 UTC, the leading line had lost organization, while the arrow became the new bow echo (Fig. 6d), and by 0500 UTC, new convective cells began to form behind this new bow echo, as the system propagated toward the south (Fig. 6e). By 0700 UTC, the leading bow echo weakened as the new arrow extended behind and to the west of the bow, across northwest Indiana and Illinois to connect with a third MCS, evident over Iowa (Fig. 6f). The second bow and arrow system then remained stationary while losing organization, as the third MCS swept through the area, merging with the original system, before they both (as one system) moved off toward the northeast (not shown).

The 500-hPa analysis (not shown) indicates a 500-hPa shortwave over Idaho and Montana at 1200 UTC 4 July, which moved eastward and lead to convection initiation over the Midwest and Great Lakes regions. An 850-hPa nocturnal low-level wind maximum (with wind speeds up to 20 m s^{-1}) existed from the Gulf of Mexico into the central United States at 1200 UTC 4 July and 0000 UTC 5 July, with the winds turning to southwesterly and westerly over the upper Midwest. This brought warmer, moist air into this region, creating a more-unstable environment.

As noted above, the bow and arrow occurred in two separate phases during this event. There was a prominent arrow evident around 0200 UTC, as well as 0700 UTC. Figure 7 shows surface analysis for 0200 UTC, which is generally representative of both time periods. A strong bow echo was located over western Ohio, while an organized arrow extended northwestward, from the cold pool in western Ohio to the Illinois–Indiana border.

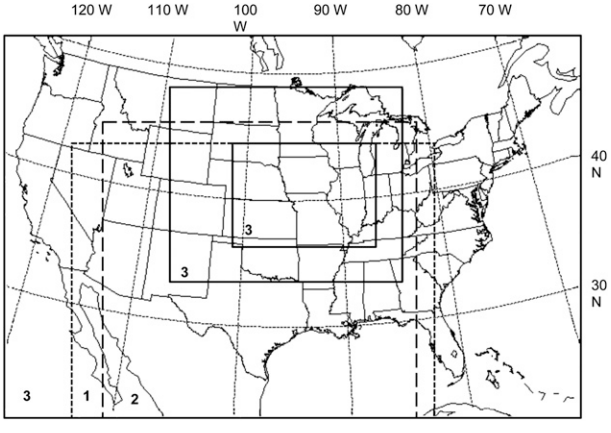

FIG. 5. Composite of gridded domains used for model simulation for cases 1, 2, and 3. Numbers are inside the bottom left-hand corner of each domain to indicate, which case the domain represents. Case 1 (thin dashed lines) and case 2 (thick dashed lines) each use one large high-resolution domain, and case 3 (solid black lines) is run with a large coarse mesh domain that includes two nested grids.

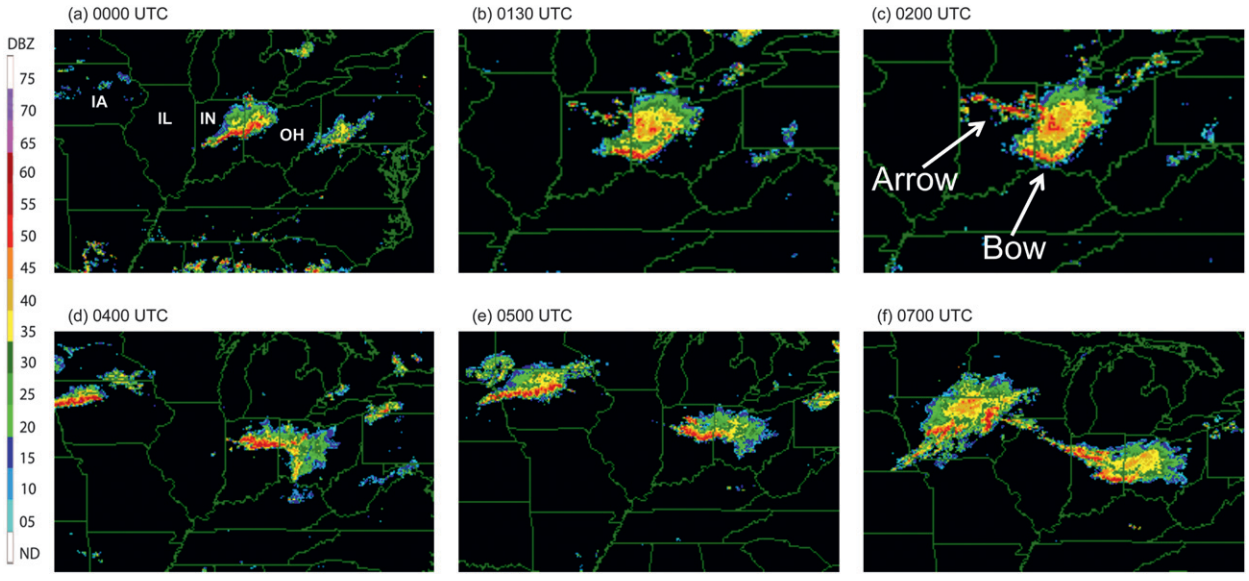

FIG. 6. Composite radar reflectivity progression at (a) 0000, (b) 0130, (c) 0200, (d) 0400, (e) 0500, and (f) 0700 UTC 5 Jul 2003.

A 1018-hPa mesohigh (Fujita 1955) was located near the leading edge of the convective line. It appears that the area of high pressure actually crossed the leading edge into the area ahead of the bow; however, this is most likely due to objective analysis of coarse surface observations. The mesohigh was generally contained behind the leading edge, as has been previously exemplified as a characteristic for bow echo environments (Fujita 1955; Hamilton 1970; Johnson and Hamilton 1988). Isotherms reveal an intense cold pool behind the bow echo, with a temperature drop of 5°–10°C across its leading edge. There appears to have been a west–east baroclinic zone across the region, which may have contributed to the overall abundance of convective activity; however, the development of the arrow as a narrow line at an angle to the baroclinic zone suggests that other mechanisms were responsible for creating the arrow. The surface winds were southerly near the convective arrow in northern Indiana. Based on this surface analysis, there was negligible temperature advection or convergence at the surface within the cold pool in the area where the arrow developed; therefore, convection in this arrow cannot be attributed to these surface-based lifting mechanisms. This type of elevated convection may be associated with a particular type of horizontal mass convergence, which is displaced above the boundary layer or cold pool, discussed by Banacos and Schultz (2005).

From observational analysis for this case, several aspects of the environment, including the midlevel shortwave and the low-level wind maximum and associated temperature and moisture advection, are identified and explain the development and maintenance of organized convection from a synoptic standpoint. However, the available data are insufficient to determine the mesoscale mechanisms responsible for initiating and maintaining the convective arrow behind the bow echo, nor the reason for the orientation of the arrow. To address these issues a numerical simulation of this event was attempted, but was unfortunately unable to satisfactorily reproduce the observed convective structure (as was the case with several of the 14 events, which is potentially indicative that the predictability of these cases is low). However, the next three cases that will be discussed are successfully simulated, which enables detailed mesoscale analysis.

b. Synoptic and mesoscale observations of the simulated cases

Case 1 began on the afternoon of 17 June 2006 (around 2000 UTC). As an MCS moved eastward out of Texas another strong line of convection formed along the south-central Oklahoma and north-central Texas border (Fig. 8a). By 0300 UTC on 18 June, the convection had moved southward, into north-central Texas, and organized into a bow echo (Fig. 8b). Around 0500 UTC, the first cells of the convective arrow appeared (Fig. 8c). The arrow had fully organized by 0600 (Fig. 8d), before it lost organization by 0700 (not shown). The bow echo maintained organization and continued to move toward the east.

Case 2 occurred on 8 May 2009, with an arrow developing behind the derecho-producing bow echo analyzed by Coniglio et al. (2011). Around 0154 UTC

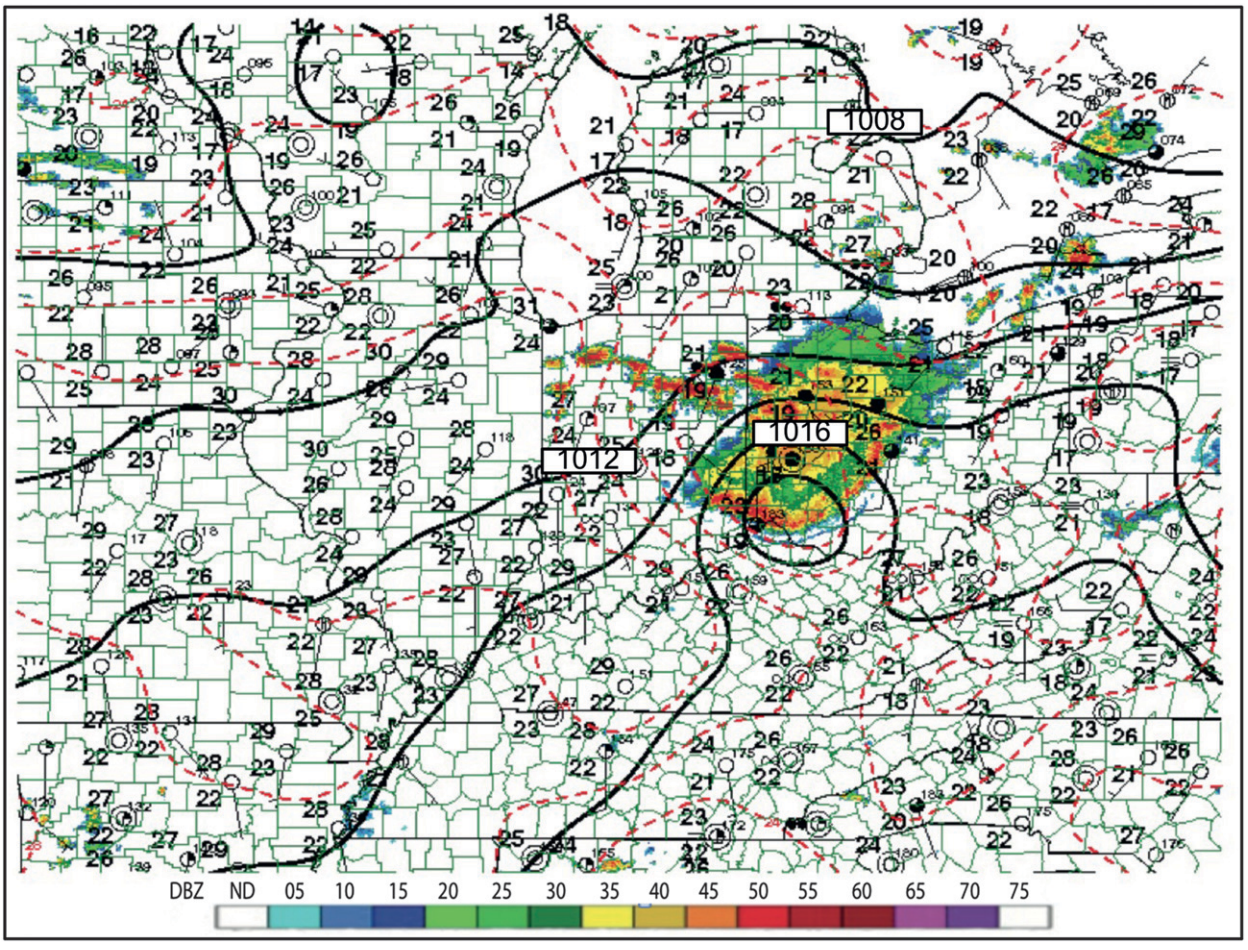

FIG. 7. Surface analysis for 0200 UTC 5 Jul 2003. Overlays of composite radar reflectivity (shading, dBZ), mean SLP (solid black lines, every 2 hPa), temperature contours (dashed red lines every 2°C), and surface stations that show temperature (°C), dewpoint temperature (°C), pressure (hPa), and wind direction and speed (kt).

8 May, scattered weak convection began to form over northeastern Colorado (Fig. 9a). Over the next several hours, the system moved southeastward and by 0754 UTC, an organized line of convection gathered over central Kansas (Fig. 9b). By 1155 UTC the leading line of convection had progressed into a strong bow echo near the border between southeastern Kansas and central Missouri, extending into northeastern Oklahoma (Fig. 9c). Around 1527 UTC, convection began to form behind the bow echo (not shown), and exhibited an organized arrow by 1725 UTC (Fig. 9d) near the Missouri–Arkansas border. The system later lost organization, as a whole, as it moved off toward the northeast.

Case 3 occurred on 15 September 2010. Around 2200 UTC 14 September, a small area of convective cells was evident over northeast Colorado. By 0355 UTC 15 September, the system had advanced eastward into northwest Kansas, having strengthened and organized into a convective line with an arrow located to its rear (Fig. 10a). As the MCS evolved its leading edge became bow shaped, while the southeast–northwest-oriented arrow to its rear had increases in radar reflectivity (Fig. 10b). The bow strengthened while the arrow was maintained as the MCS moved east-southeast over the next several hours, until the system lost some of its organization around 1200 UTC (Fig. 10c). By 1257 UTC the system had reorganized in northeast Kansas, and exhibited another well-defined convective arrow (Fig. 10d). Over the next few hours the bow strengthened and moved south into east-central Kansas, as the arrow turned and became parallel to the bow echo (Fig. 10e), and then dissipated by 1630 UTC. By this time, the lingering arrow, still maintaining its west–east orientation, redefined the leading edge of the MCS, which now had a new arrow behind it. This redeveloping MCS strengthened, maintaining the arrow, and moved into

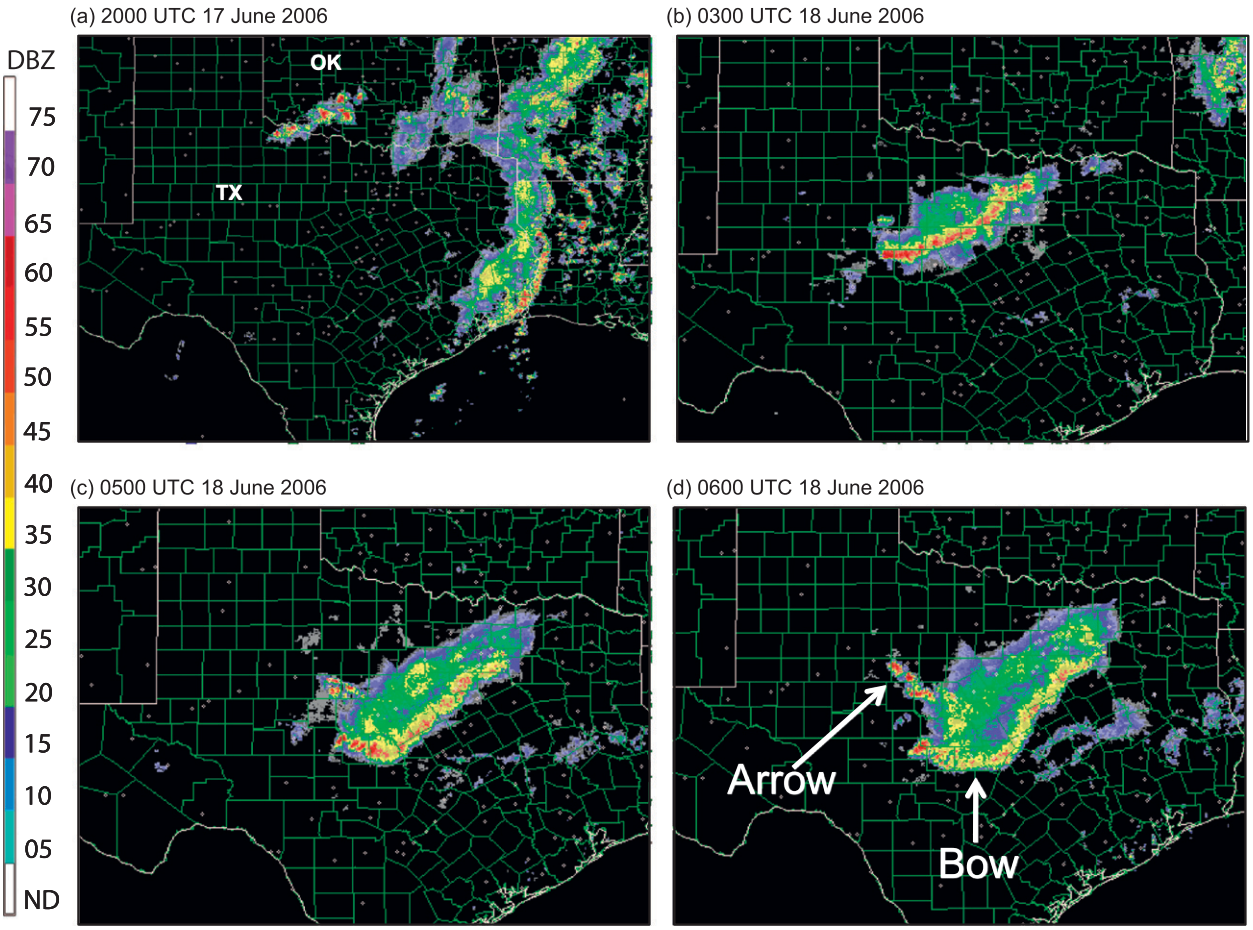

FIG. 8. Composite radar reflectivity progression from (a) 2000 UTC 17 Jun 2006, and at (b) 0300, (c) 0500, and (d) 0600 UTC 18 Jun 2006. The area shown in (a) is different from that in (b)–(d).

central Missouri (Fig. 10f), before losing organization around 2230 UTC.

For these three cases, there is sufficient evidence in synoptic-scale upper-level and surface analyses to show that the ingredients for producing deep convection (e.g., Johns and Doswell 1992) were present. Large-scale ascent ahead of a 500-hPa shortwave is implied in Fig. 11a for case 1, and warm air advection (WAA), where $-\mathbf{V} \cdot \nabla\theta > 0$, is evident in all three cases at the 850-hPa level (Figs. 11b,d,f). Furthermore, a low-level jet (LLJ), which increased relative humidity and thermodynamic instability over the region, is evident in all three cases (Figs. 11b,d,f). In addition to these similarities, some notable differences among cases were found. In contrast to the strong shortwave trough in case 1, cases 2 and 3 occurred under mainly zonal flow (Figs. 11c,e). At the surface, a prominent dryline was located just west of the convective region in case 1, and a jet streak existed at 300 hPa in case 3 (not shown), neither of which occurred in the other two cases.

To further generalize the observed MCS environment, storm-centered composites of 500-hPa heights and winds and 850-hPa temperature and winds for all 14 bow and arrow cases identified for this study are shown in Fig. 12. These composites are created using the North American Regional Reanalysis (NARR; Mesinger et al. 2006) by defining a 71 × 71 (approximately 2300 km × 2300 km) grid centered at the latitude, longitude, and time nearest the development of each arrow, and then performing composite analysis on those grids. Though a weak trough is evident in the 500-hPa height composite over Kansas and Oklahoma, stronger shortwaves from individual cases are highly attenuated by the averaging, resulting in an even more general zonal flow pattern (Fig. 12a). The 850-hPa composites reveal winds transporting warm, moist air northward from the Gulf of Mexico (Fig. 12b). This aids in destabilizing the environment after the bow echo has passed. Additionally, pronounced deformation exists over the central plains. Augustine and

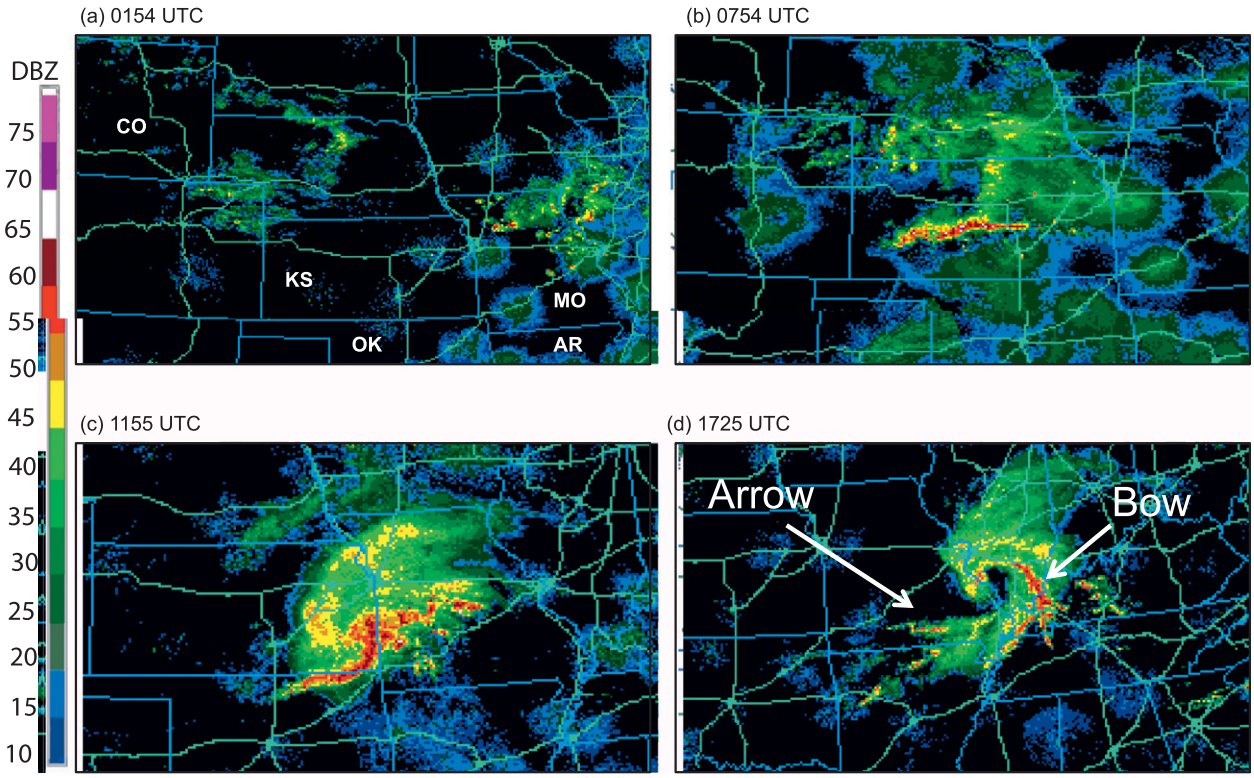

FIG. 9. Composite radar reflectivity progression at (a) 0154, (b) 0754, (c) 1155, and (d) 1725 UTC 8 May 2009.

Caracena (1994) noted that the association of this with lower-tropospheric frontogenesis was also found to be associated with stronger nocturnal MCSs in their climatology, and furthermore, when this exists, in addition to strong zonal flow aloft, it is more common for bow echoes to form.

As in the 5 July 2003 case, surface analyses overlaid with radar reflectivity are examined for cases 1, 2, and 3 (Fig. 13) at times when an arrow is evident. A fairly strong cold pool with temperatures increasing outward from this region is evident for each case, with a strong mesohigh associated with the cold pool in case 3 and evidence of wake lows (e.g., Johnson and Hamilton 1988) in cases 1 and 2. Surface winds near the developing arrow reflected outflow in cases 1 and 3, and because of the low density of surface observations, it is difficult to determine wind direction near the arrow region for case 2. More specifically, the role of surface features (such as outflow boundaries) in the initiation and orientation of the arrows in each of these three cases is not obvious.

c. Precipitation

A combination of rain gauge data and hourly estimates of composite radar reflectivity (Lin and Mitchell 2005) are used to estimate precipitation amounts from these cases (Fig. 14). They are 3-h precipitation estimates from radar, and can be compared with the observed radar reflectivity (Figs. 6, 8, and 9) during these 3-h time periods. It is evident the pattern of rainfall estimates coincides with radar reflectivity during these times. For three of the cases (5 July 2003, case 1, and case 3), precipitation analyses show that in areas that received the greatest amount of rainfall (due first to the passage of the bow echo, and then the trailing convective arrow), amounts ranged from 50 to 100 mm. In case 2 rainfall totals were only between 25 and 50 mm, and although less than the other three cases, it is still a substantial amount, that can produce flooding in the arrow region, given the antecedent moistening of the ground by the heavy rain from the bow.

4. Analysis of numerical model simulations

Numerical model simulations are used to analyze the details in the mesoscale environment of cases 1, 2, and 3. In all three simulations, a bow-and-arrow developed that resembled observations, although there were errors in the timing and location (cf. Figs. 15a and 8d, Figs. 15b and 9d, and Figs. 15c and 10f). Since the purpose of this study is to examine processes governing the formation of

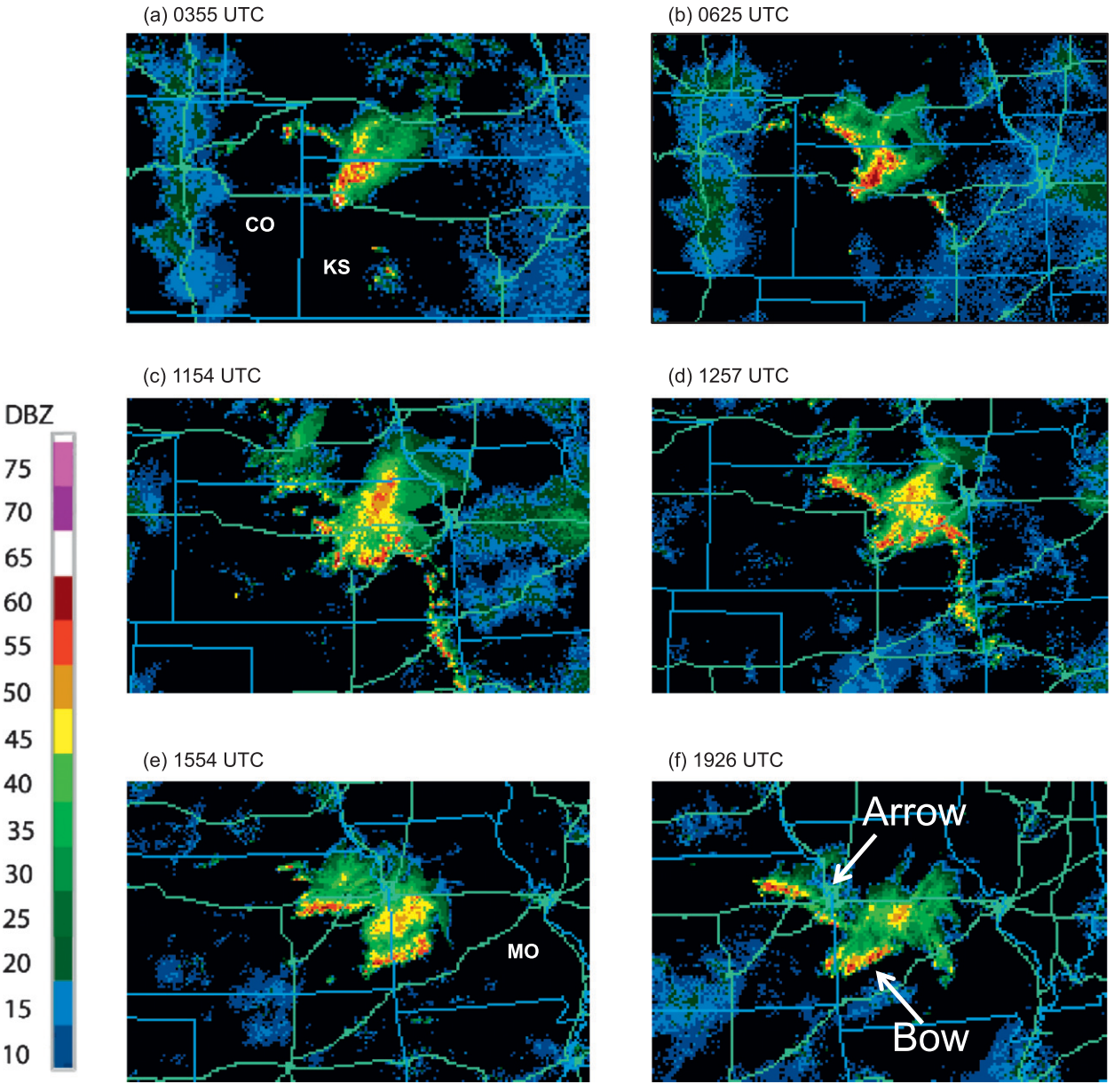

FIG. 10. Composite radar reflectivity progression at (a) 0355, (b) 0625, (c) 1154, (d) 1257, (e) 1554, and (f) 1926 UTC 15 Sep 2010.

the arrow, the simulations are useful despite these displacement and timing errors.

An important aspect of understanding environments of the bow and arrow systems is determination of the origin of updraft air parcels, which is accomplished by calculating backward trajectories over several hours. To determine the exact location of updrafts in the simulations, vertical motion plots are analyzed. Several levels near 500 hPa are tested to determine typical levels of strongest updraft vertical velocity in the arrow region. Once the level of strongest updraft vertical velocity is located, three-dimensional trajectories are then calculated for several hours backward in time, starting from the updraft centers for the three cases (Fig. 16). All three simulations show that the air parcels rising in the convective arrow primarily originate from the southwest, with case 1 having additional air parcels that originate from the west (Fig. 16a). Back trajectories presented in the X–Z plane (Fig. 17) reveal the levels and horizontal locations at which lifting occurs. From these trajectories, it is evident that the vertical locations of the parcel source regions vary. Case 1 (Fig. 17a) has parcels starting at several different levels, with seemingly random subsequent

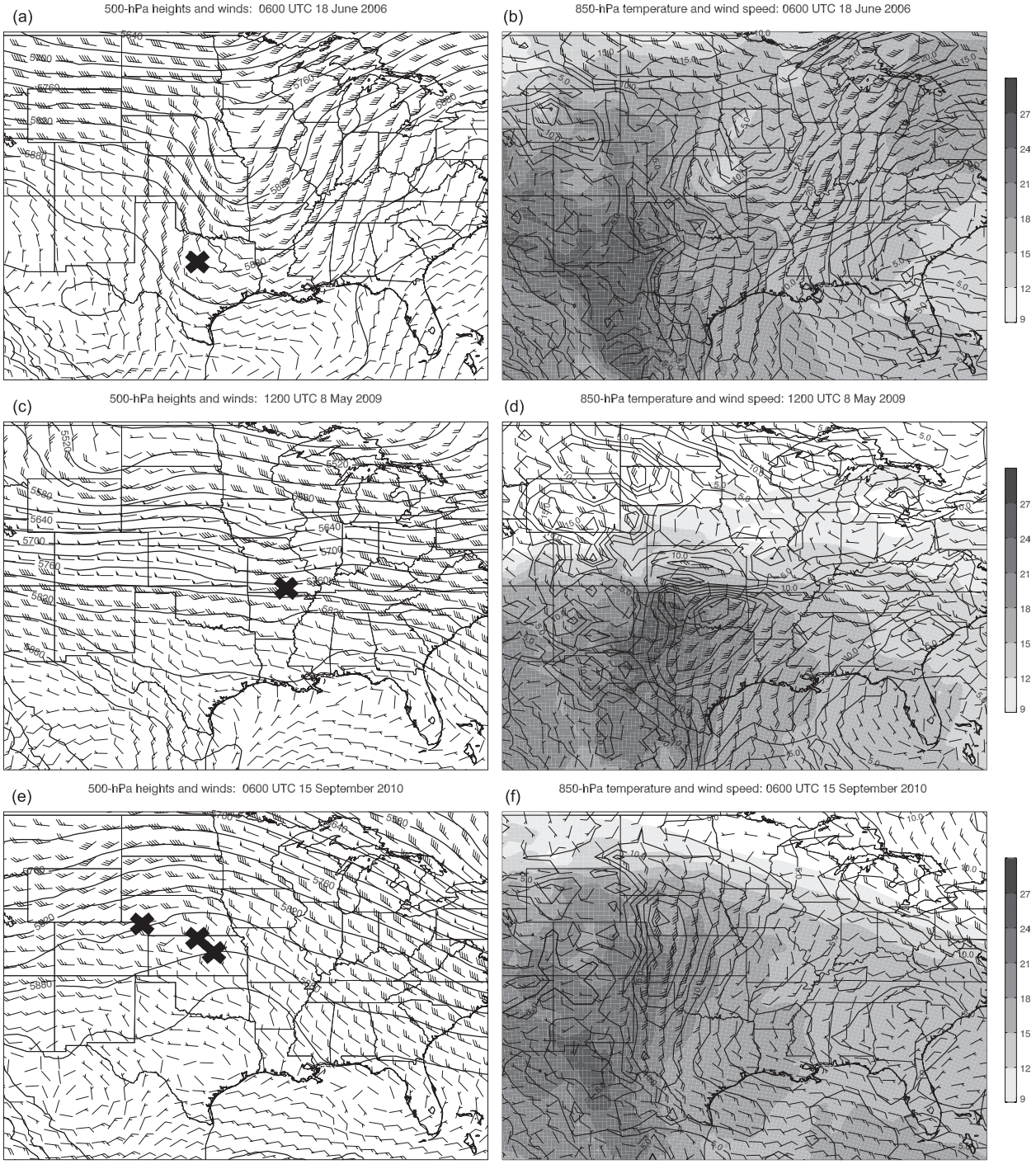

FIG. 11. NARR (Mesinger et al. 2006) 500-hPa heights and winds for (a) 0600 UTC 18 Jun 2006, (c) 1200 UTC 8 May 2009, and (e) 0600 UTC 15 Sep 2010. (b),(d),(f), As in (a),(c),(e), but for 850-hPa temperature and winds. Winds in (a),(c),(e) are represented by barbs with short barb = 2.5, long barb = 5 , and pennant = 25 m s^{-1}. Winds in (b),(d),(f) have short barb = 5, long barb = 10, and pennant = 25 m s^{-1}. Temperature (°C) in (b),(d),(f) are indicated by shading. A black "X" in (a),(c),(e) to indicates where each arrow formed for the three events.

vertical excursions before more sharply and coherently rising in deep updrafts during the last 1–2 h. Parcels for case 2 start around the 900- and 850-hPa levels, then rise rapidly to a near 700 hPa between 1100 and 1200 UTC as they ascend over the surface-based cold pool. They then undergo weak ascent or quasi-horizontal motion before making a sharp ascent in the final hour. For case 3, parcels begin slightly

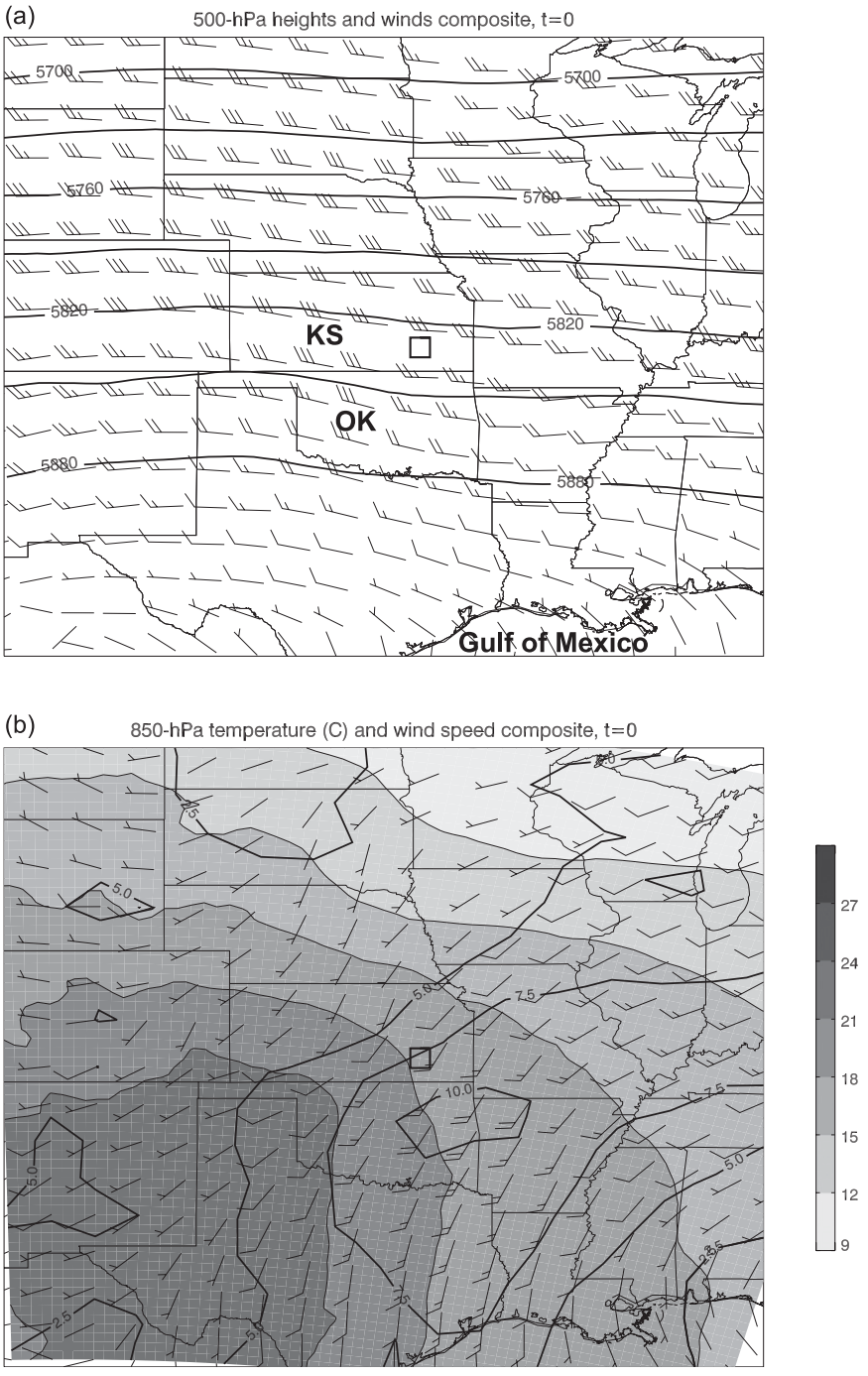

FIG. 12. As in Fig. 11, but these are storm-centered composites of all 14 cases used in this study. A blank square is marked on each figure to represent the center of the storm. The geographic background is shown only to provide an indication of the spatial scale. The method for the composite analysis is described in the text.

higher, between 800 and 700 hPa. From there they rise gradually before (as in other cases) making their sharp ascent into the updraft region during the final hour.

a. Case 1

The surface outflow boundary at 0400 UTC (Fig. 18a) extends from near the Texas–New Mexico border,

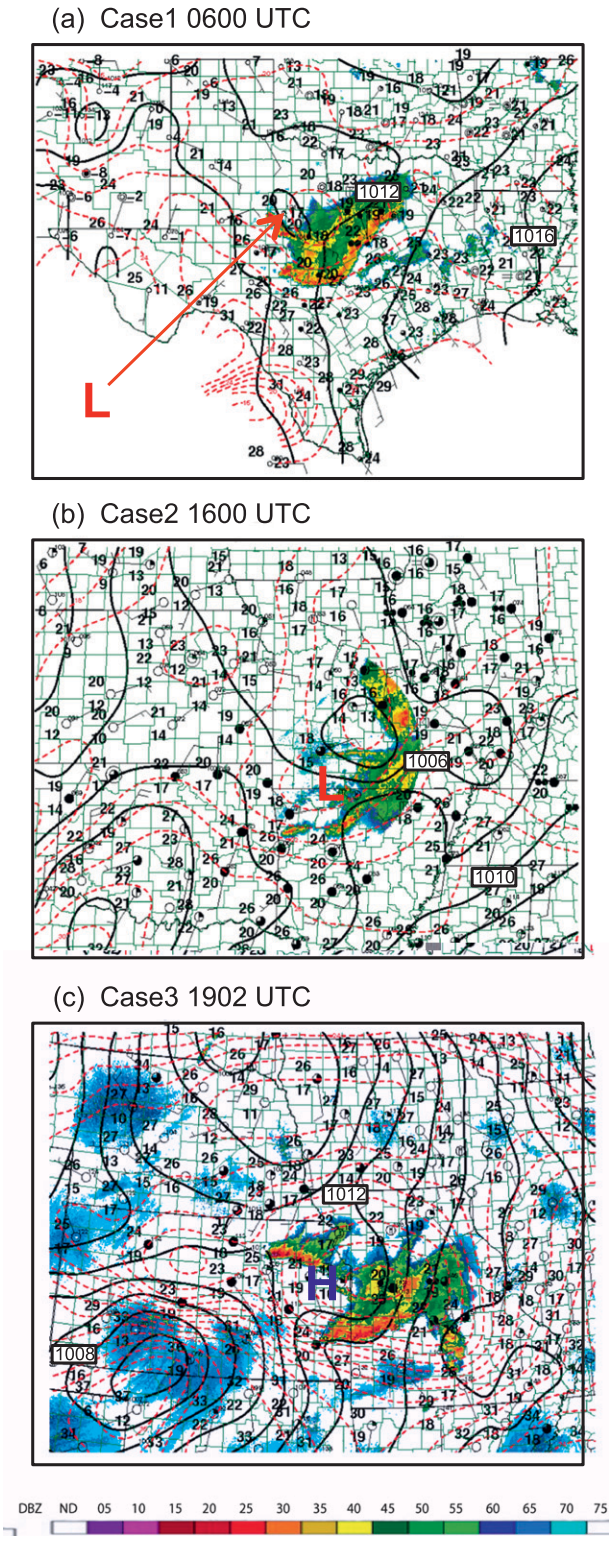

FIG. 13. As in Fig. 7, but for (a) 0600 UTC 18 Jun 2006, (b) 1600 UTC 8 May 2009, and (c) 1902 UTC 15 Sep 2010. [Mean SLP is plotted every 1 hPa in (c).]

eastward into southeast Texas, and then northward to the Texas–Arkansas–Louisiana borders. Surface winds behind the bow echo are easterly as they approach the outflow boundary, and are northeasterly beyond the western edge of the boundary. When compared to Fig. 15a, it is clear that the convection in the arrow is not a direct result of lifting associated with that of the outflow boundary, as it is not occurring anywhere near the edge of the cold pool. Comparison of Fig. 18a to observational surface analysis (Fig. 13a) reveals consistency, as they both show similar wind direction, as well as a temperature gradient, illustrating the cold-pool and outflow boundary.

Recall that parcels ending up in the convective arrow originated in two different locations for this case. Trajectories from both the west and southwest originate around the 850-hPa level; therefore, this pressure level is used to analyze possible lifting mechanisms associated with temperature advection and/or wind variations. At 0200 UTC (Fig. 18b), WAA is occurring behind the bow in central Texas. Winds in south-central Texas are from the southwest, while winds in north Texas and Oklahoma are from the north. This results in convergence in the region where the convective arrow develops, which, in addition to the isentropic lift, may help to enhance upward motion and resulting convection. A westerly rear-inflow jet is also apparent behind the bow echo, as wind speeds in this location are slightly stronger than the surrounding winds (from 7 to 13–16 m s^{-1}). This horizontal shear is strongly deformational and may be responsible for maintaining linearity of the arrow.

Several parcels make a sharp ascent near the 700-hPa level within the final hour of the back-trajectory calculation. Figure 18c shows that again at this level, there is slight convergence of winds coming from the west-southwest with those from the northwest, in the region of the updrafts. There is evidence of horizontal speed shear, cyclonic curvature, and convergence, where wind speeds from the west vary between 10 and 15 m s^{-1}, while winds from the northwest are from 15 to 18 m s^{-1}. Temperature gradients in this area are stronger, resulting in stronger WAA.

Frontogenesis at 900 hPa, overlaying composite radar reflectivity is shown (Fig. 18d) in an effort to determine whether frontogenetically forced ascent is responsible for convective cell development in the arrow. At the time in this figure cells in the arrow are newly initiated. It is evident there is very strong frontogenesis occurring at the outflow boundary, both at the surface (not shown) and aloft (Fig. 18d). In the vicinity of the developing arrow, there is little frontogenesis at the surface (not shown), but there is a secondary frontogenesis

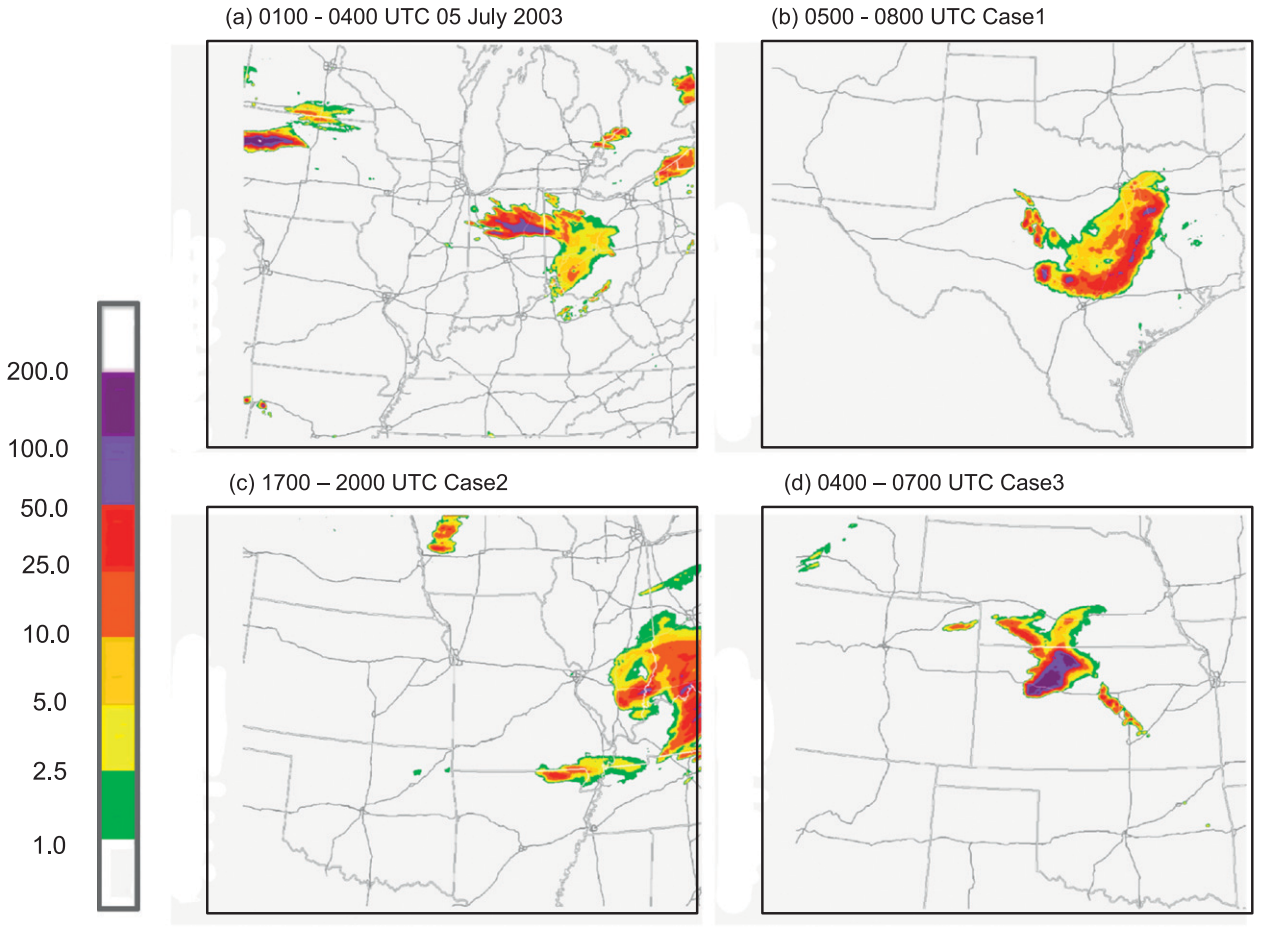

FIG. 14. Analysis of 3-h estimated precipitation (mm) for (a) 0100–0400 UTC 5 Jul 2003, (b) 0500–0800 UTC 18 Jun 2006, (c) 1700–2000 UTC 8 May 2009, and (d) 0400–0700 UTC 15 Sep 2010.

maximum at 900 hPa (Fig. 18d). Although the magnitude of frontogenesis is much smaller near the arrow than it is near the outflow boundary, it does still exist, showing that initiation of convection in the arrow is linked to convergence occurring in the presence of a temperature gradient.

To obtain a thermodynamic perspective of the environment, vertical cross sections of potential temperature overlaid with CAPE are analyzed (Fig. 19a), and show an unstable environment with CAPE close to 1500 J kg^{-1} for both surface-based and elevated air parcels approaching from the southwest. Gradual approximate isentropic lifting (which, for steady conditions, is equivalent to WAA) is illustrated for parcels moving from the southwest to northeast, just above the surface. Evidence of a cold pool exists near the surface on the right-hand side, while strong vertical motion is displayed as air approaches this cold pool. This is consistent with the findings of Trier et al. (2010), in which they used similar analyses to study the diurnal cycle for warm-season precipitation. They found that the most intense convection in back-building nocturnal MCSs occurred in areas where more gradual isentropic lifting was occurring above the cold pool below. Furthermore, they found sharper lifting that occurred far behind the cold-pool edge in areas where the LLJ and gradual isentropic ascent above the stable air, under the frontal surface were contributing to the most intense convection.

As the bow echo passes through the region where the arrow would form, it removes all CAPE as a result of the overturning of air, in addition to evaporative cooling of descending air in the outflow from the bow (Fig. 19b). An hour later, however, the bow echo is farther southeast, and CAPE has returned, with a value between 1500 and 2000 J kg^{-1} for the two updraft locations farthest west (Fig. 19c). The third updraft location is still too close to the bow echo outflow to acquire enough instability by this time, but sufficient CAPE returns prior to convection initiation (not shown). A time series

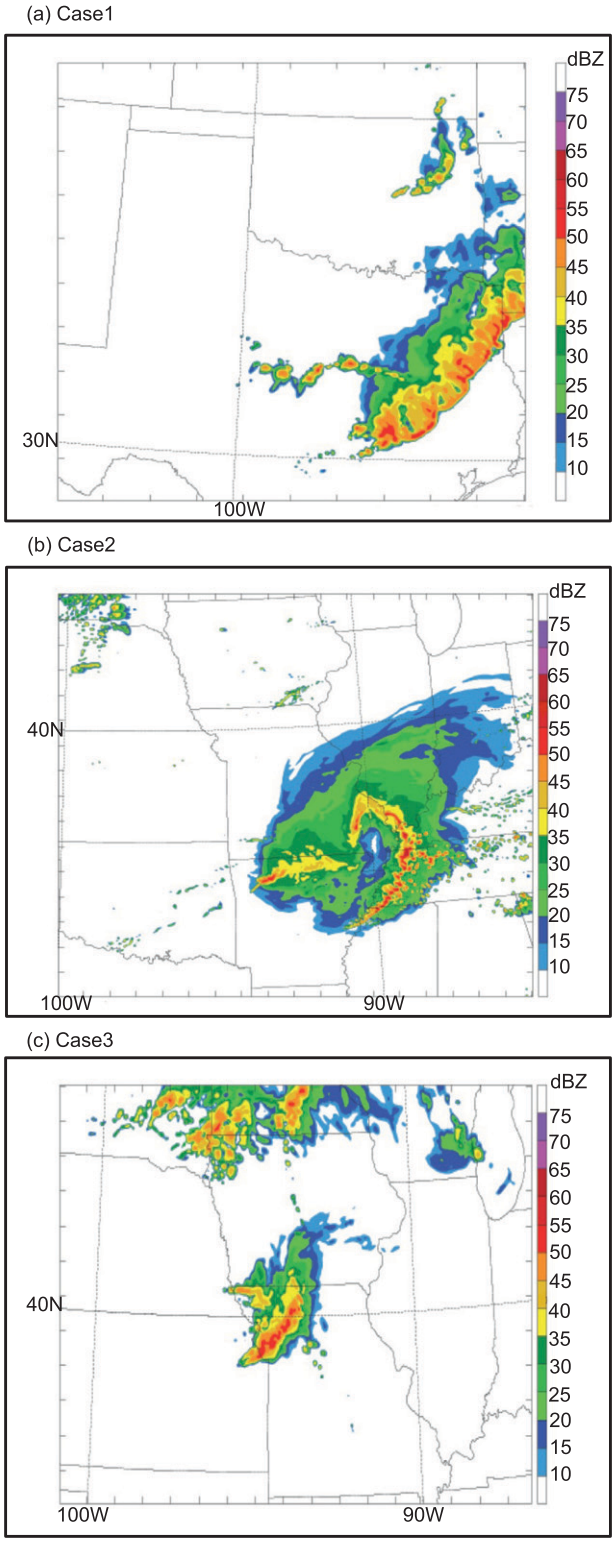

FIG. 15. WRF numerically simulated radar reflectivity for (a) 0400 UTC 18 Jun 2006, (b) 1630 UTC 8 May 2009, and (c) 1700 UTC 15 Sep 2010. Colors represent reflectivity in increments of 5 dB*Z*.

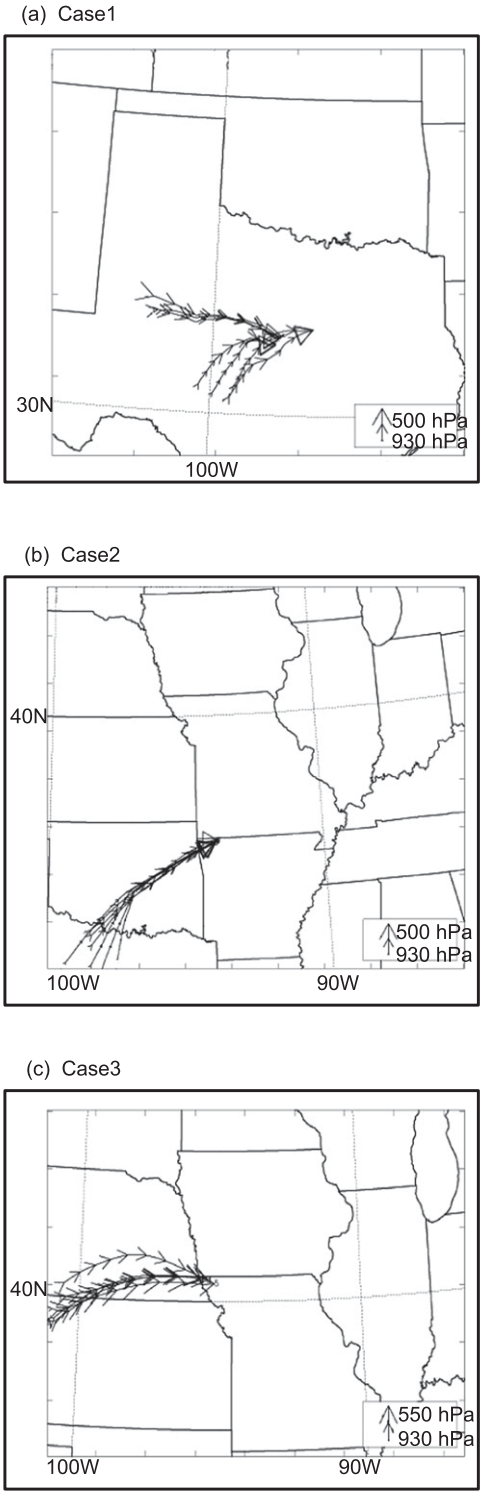

FIG. 16. Back trajectories in the *X*–*Y* plane for (a) 0400 UTC 18 Jun back to 2100 UTC 17 Jun 2006, (b) 1445 back to 0800 UTC 8 May 2009, and (c) 1700 back to 0900 UTC 15 Sep 2010. Each trajectory represents one parcel, while each arrowed notch represents 1 h.

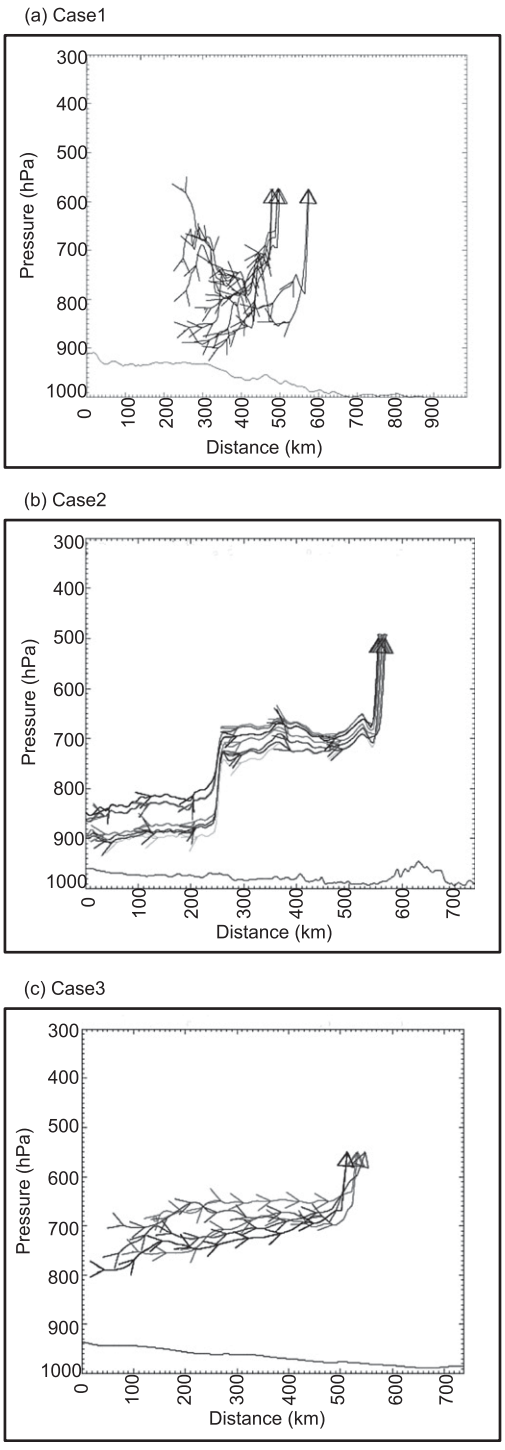

FIG. 17. As in Fig. 16, but here the X axis represents horizontal distance, while the Z axis represents pressure level (hPa). The horizontal cross section for these trajectories is taken by visually averaging the trajectories shown in Fig. 16, for each case. This is the same cross section given in Figs. 19b, 21b, and 23b.

(Fig. 20a) confirms the foregoing findings that most unstable CAPE (MUCAPE) is initially high, decreases to nearly zero after the passage of the bow echo, but then recovers somewhat, to provide a fairly unstable environment in which the arrow is initiated. The return of instability is likely due to a combination of the LLJ bringing warm, moist air into the region, and the gradual isentropic lift helping to condense parcels, destabilizing the environment. When this instability is combined with the frontogenesis and shear mentioned above, it can produce an arrow behind a bow echo.

b. Case 2

Surface analysis at 1400 UTC (Fig. 21a) reveals features similar to those of case 1 (Fig. 17a), in which the edge of the cold pool extends much farther west of the area in which the strongest vertical motion appears, indicating that the outflow boundary is not directly responsible for the final phase of strong lifting that initiates convection in the arrow region. Again, the simulation agrees with the surface analysis of observations (Fig. 12b), both having south-southwesterly winds south of a strong convectively induced cold pool.

The 900- and 850-hPa levels are analyzed for this case since the parcels rising in the arrow all begin near these two levels (Fig. 15b). At 1150 UTC the 900-hPa air parcels that later rise within the arrow are located in southwesterly flow at the edge of the cold pool behind the bow echo (Fig. 21b). Here, the cold-pool boundary likely influences the first of the sharp vertical displacements along the trajectories of Fig. 15b. The flow structure is similar at 850 hPa (Fig. 21c) with southwest flow also arriving at the cold-pool boundary. At this level, a strong LLJ is evident with a 25 m s^{-1} wind speed maximum.

The strong southwesterly LLJ persists though 1445 UTC (Fig. 21d). It also appears that winds north of the arrow are coming from the northern bookend vortex (e.g., Weisman and Davis 1998) of the bow echo. The winds start from the east, wrapping around, becoming northerly, then westerly into the rear-inflow region behind the bow. These winds create convergence with ambient southwesterly winds. Additionally, winds in the rear-inflow region are faster (25–29 m s^{-1}) than the surrounding winds (8–10 m s^{-1}), indicative of the rear-inflow jet. Isotachs show a distinct line of faster winds in the location of the arrow region, indicating horizontal speed shear, which may lead to deformation, supporting the linearity of the arrow.

The 700-hPa analysis is shown for 1400 UTC (Fig. 21e) since the parcels enter convective updrafts in the arrow region from this level around this time. The arrow occurs within a broader zone of WAA. Southwest flow

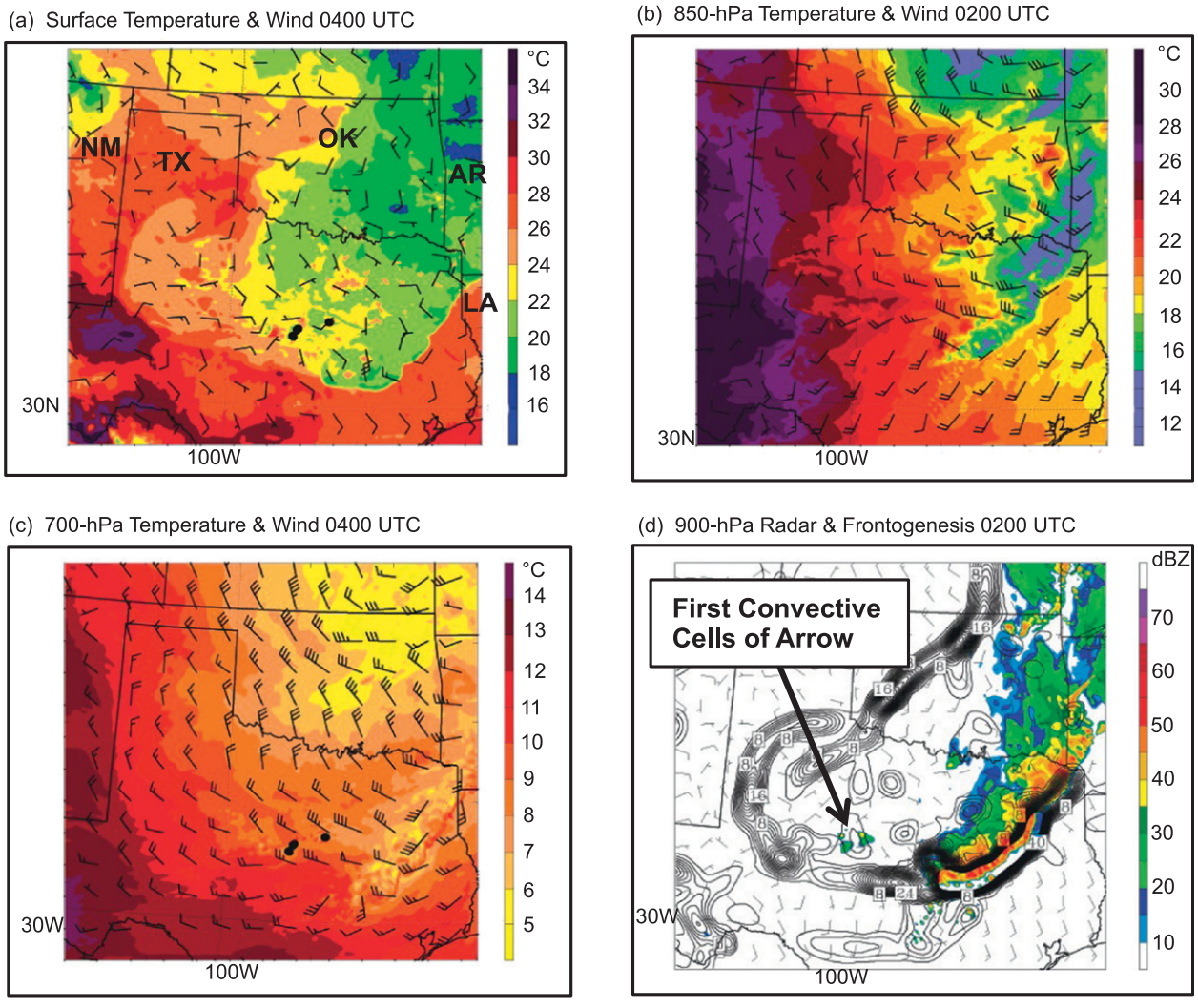

FIG. 18. Temperature and wind fields for case 1 (18 Jun 2006) at the (a) surface at 0400 UTC (b) 850-hPa level at 0200 UTC, (c) 700-hPa level at 0400 UTC, and (d) composite radar reflectivity and frontogenesis for 900-hPa at 0200 UTC. Colors represent temperature (in increments of 1°C), while wind speed and direction is represented using wind barbs, where short barb = 2.5 m s^{-1}, long barb = 5 m s^{-1}, and pennant = 25 m s^{-1}. Black bullets plotted on (b),(c) indicate the areas of greatest updrafts within the arrow, which occurred at this time (0400 UTC). Radar reflectivity in (d) is represented by colors, in increments of 5 dB*Z*, and frontogenesis is given in black contours in increments of 2 K $(100\ km)^{-1}\ h^{-1}$.

transports warm air from Oklahoma into the arrow region where it converges with west-northwest flow. Again, there is strong frontogenesis at the outflow boundary, with a secondary maximum near the developing convective cells in the arrow (Fig. 21f).

As for case 1, thermodynamic analysis is performed (Fig. 22a) showing there is no CAPE for surface-based parcels in the area where the arrow would develop, but large CAPE (values >3500 J kg^{-1}) for elevated parcels, where lifting begins. In addition, the vertical cross section reveals gradual isentropic lifting, and then sharper lifting in the area of the updraft. Prior to 1400 UTC the cold-pool region of the bow echo is situated where the subsequent arrow develops, and there is thus no CAPE in this location (not shown). However, MUCAPE values in this area at 1400 UTC are 1000–1500 J kg^{-1}, with values >3500 J kg^{-1} toward the southwest, into central Oklahoma (Fig. 22b). Although the CAPE values in the arrow region are small relative to the prebow environment, they still indicate a return of instability, which is also reflected in the time series in Fig. 20b.

c. Case 3

Surface analysis reveals a cold pool behind the simulated bow echo (Fig. 23a) but is less widespread than in

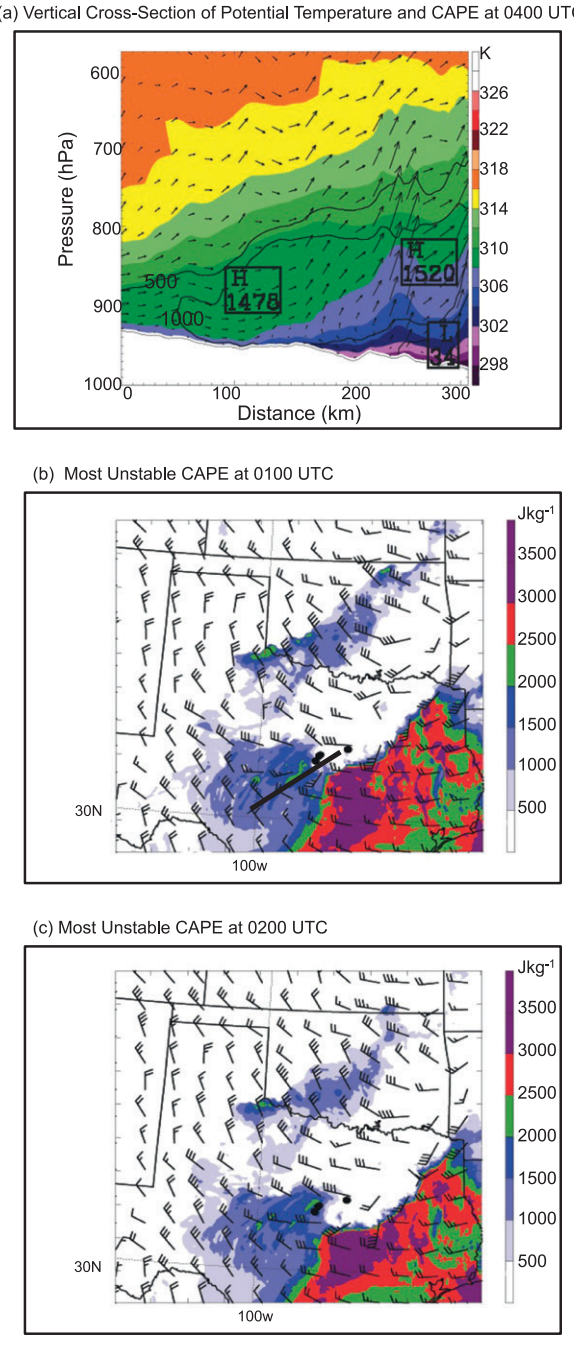

FIG. 19. (a) Vertical section of potential temperature and CAPE for parcels lifted from each level at 0400 UTC 18 Jun 2006. Potential temperature is shown by colors in increments of 2 K; while CAPE (in increments of 500 J kg^{-1}) is represented by solid black contours. Flow vectors in the plane of the cross section are also shown. The *X* axis represents horizontal distance, and the *Z* axis represents pressure level (hPa). The horizontal location of these cross sections is given by the solid black lines shown in (b). MUCAPE for (b) 0100 and (c) 0200 UTC 18 Jun 2006. Colors represent values of CAPE in increments of 500 J kg^{-1}. Solid black contours represent boundaries for areas with no CAPE. Wind barbs express 0–6-km vector wind difference (short barb = 2.5 m s^{-1}, long barb = 5 m s^{-1}, pennant = 25 m s^{-1}). Black bullets are plotted to indicate the exact areas of strongest updraft within the arrows.

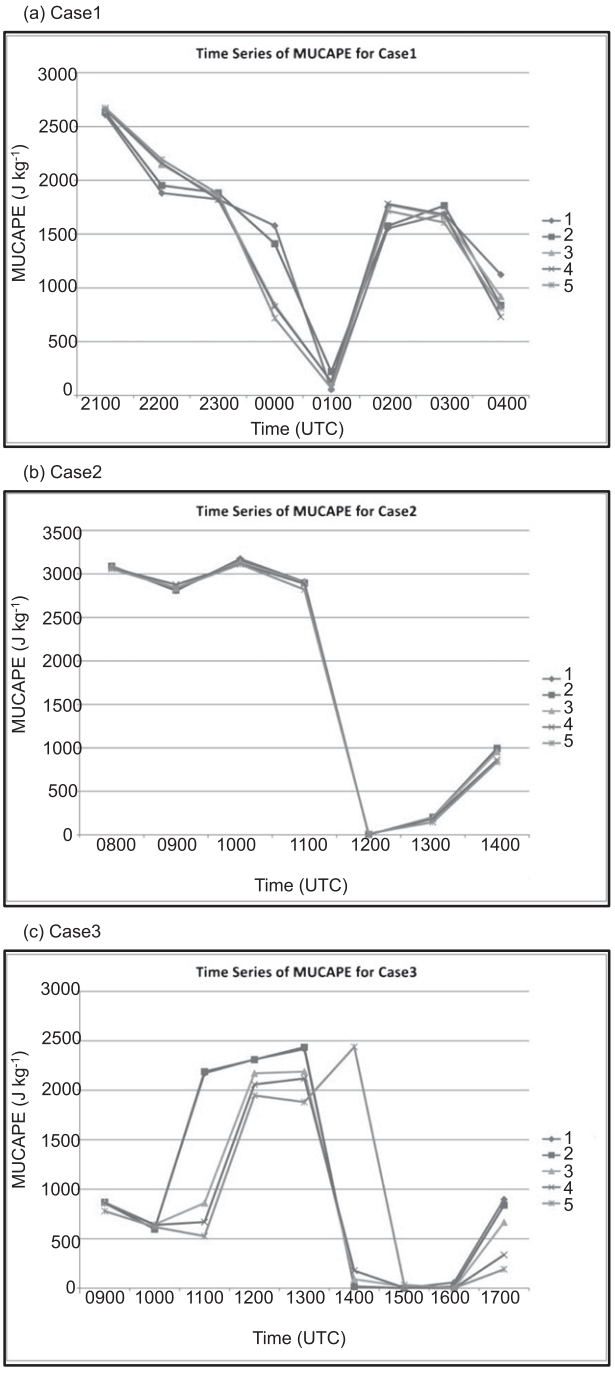

FIG. 20. Time series plots of MUCAPE for (a) 18 Jun 2006, (b) 8 May 2009, and (c) 15 Sep 2010. The *X* axis represents time (UTC) and the *Y* axis represents values of MUCAPE (J kg^{-1}). The plotted colored lines represent locations of updrafts within the convective arrow region.

the previous two cases (Figs. 17a and 21a). The 850-hPa wind speed is plotted for 1700 UTC (Fig. 23b) and shows that the arrow has formed within the southwesterly LLJ. Although the wind speed gradient (between winds

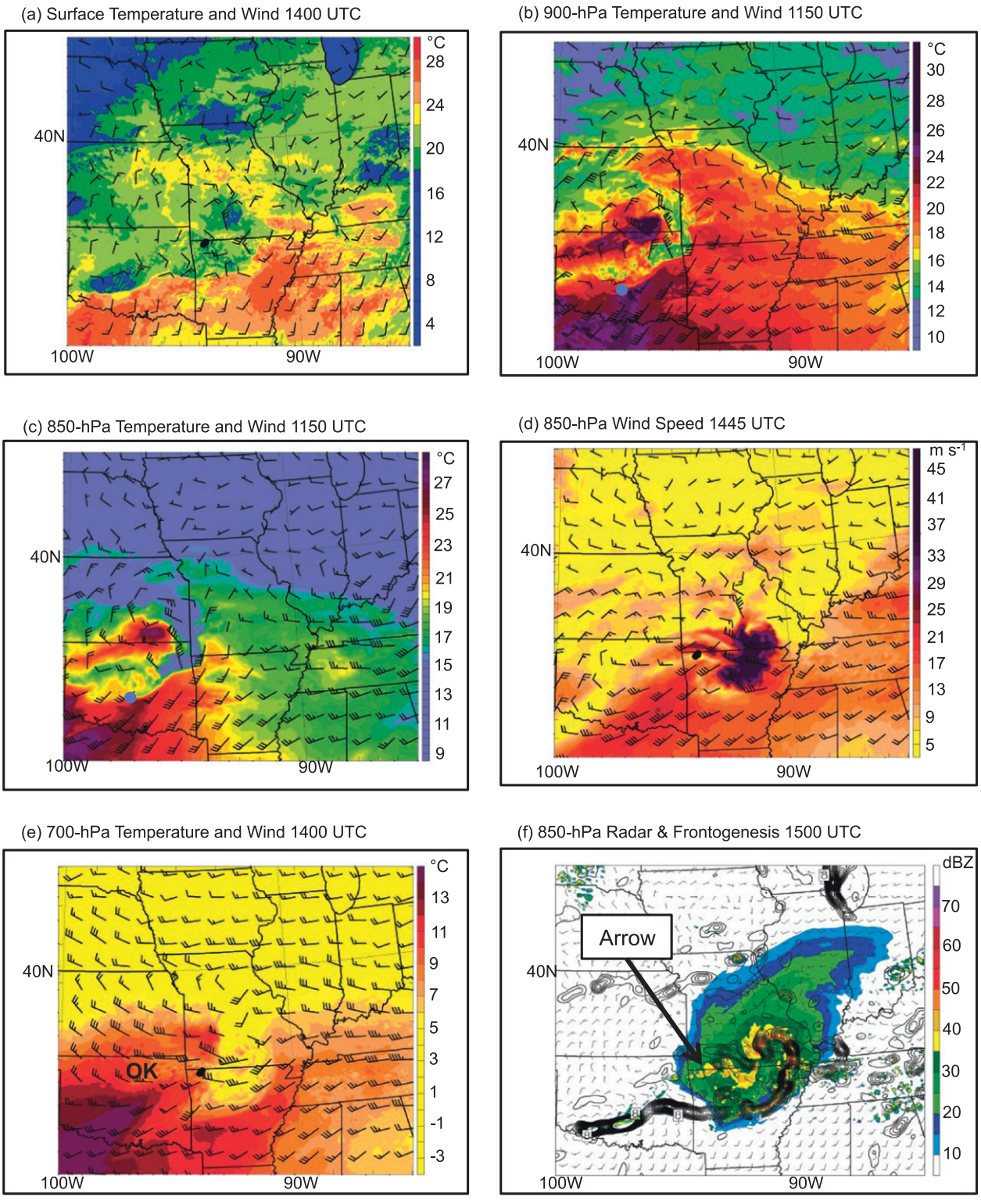

FIG. 21. As in Fig. 18, but for case 2 (8 May 2009): (a) surface temperature and wind at 1400 UTC; (b) temperature and wind for 900 hPa at 1150 UTC; (c) temperature and wind for 850 hPa at 1150 UTC; (d) wind speed analysis for 850 hPa at 1445 UTC, where colors represent wind speeds in increments of 2 m s^{-1}; (e) temperature and wind for 700 hPa at 1400 UTC; and (f) composite radar reflectivity and frontogenesis for 850-hPa at 1500 UTC. In (b) and (c), blue bullets are plotted to indicate where (along the trajectory) the parcels would be at that time. In (a),(d),(e) the black bullets are plotted to indicate the regions of greatest updraft within the arrow.

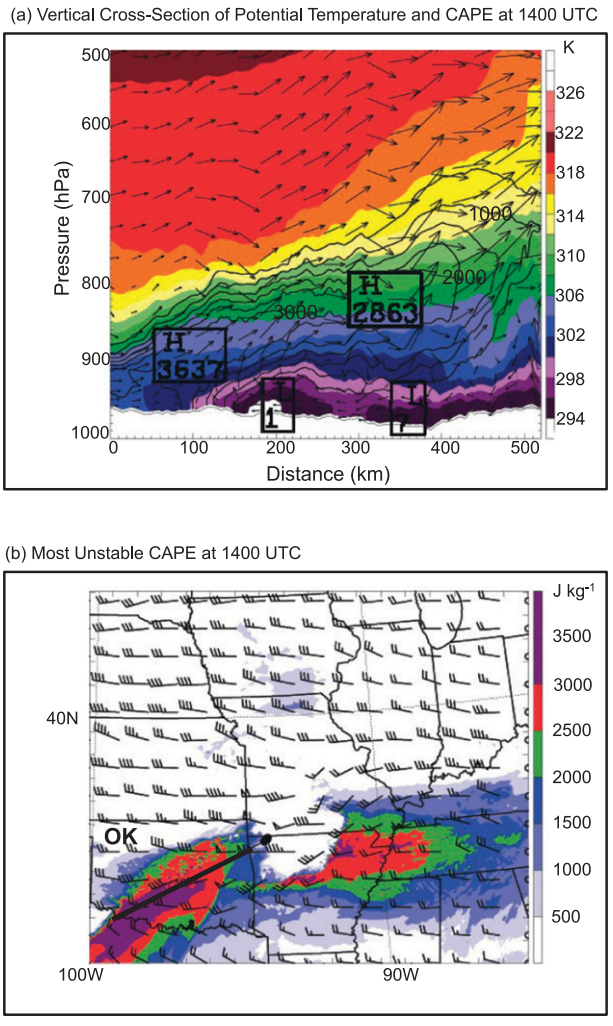

FIG. 22. (a) As in Fig. 19a, but for 1400 UTC 8 May 2009. (b) As in Figs. 19b,c, but for 1400 UTC 8 May 2009.

inside the arrow and those outside the arrow) is less than in case 2, the arrow still forms along a strong gradient, where winds increase from 14 to 20 m s^{-1} from the surrounding areas into the arrow. This horizontal wind shear begins to develop about an hour prior to this (1600 UTC; not shown) after the bow echo passes through. Like in cases 1 and 2, WAA occurs within the strong southwesterly LLJ. However, the southwesterlies at this level are more uniform in direction than in the other two cases resulting in little discernible convergence.

At 800 hPa, winds to the north of the arrow region are westerly, possibly as a result of the rear-inflow jet into the bow echo, which leads to convergence with the southwesterlies to the south (Fig. 23c). Additionally, the southwesterlies have speeds of 15–21 m s^{-1}, while the westerlies have speeds of only 13–15 m s^{-1}, which results in some horizontal speed shear, again potentially leading to the linear shape of the arrow. Figure 23e shows strong elevated frontogenesis just south of the convective arrow, indicating that it, once again, plays a large role in initiating convection in the arrow.

As mentioned earlier, all the parcels rise abruptly near the 700-hPa level within the last hour of the back-trajectory calculation. Analysis of this layer is shown for 1645 UTC (Fig. 23d), which is just prior to the time in which the updraft is most intense. Again, there is WAA in strong southwesterly flow at this level. There is also strong westerly flow in (and north of) the inflow region, into the bow. The winds from the southwest (which have speeds of 21–23 m s^{-1}) converge with westerly and northwesterly winds (with speeds from 13–15 m s^{-1}). Furthermore, wind speeds in and around the updraft locations have speeds of 23–26 m s^{-1}.

Thermodynamic plots reveal that case 3 has less CAPE than the previous cases, with its highest value just above 2000 J kg^{-1} (Fig. 24a). Parcels gradually move upward above the cold pool, and then enter a sharp updraft when they approach a region of stronger isentropic lifting. Additionally, there is evidence of surface stabilization within the cold pool, while elevated instability remains. Just prior to 1700 UTC (not shown), the updraft locations are in the stable cold-pool region; however, at this time (Fig. 24b), two of the updraft regions are shown to be in an environment with 500–1000 J kg^{-1} of CAPE. Once again, a time series (Fig. 20c) confirms that CAPE is removed as the bow echo passes, but recovers within 2–3 h.

5. Conclusions and indications for future work

A bow and arrow is a mesoconvective structure consisting of a bow echo, with a trailing quasi-stationary convective region that is perpendicular to, and above the cold-pool region behind the bow. Over the course of 12 warm seasons, 14 cases of the bow and arrow phenomenon are identified. Forecasting these events is difficult due to frequent lack of detection by NWP models, in addition to a lack of prior research explaining the causes of this phenomenon. Failure to produce accurate forecasts can lead to little or no warning for harmful consequences, such as flooding, hail, and severe wind damage, associated with bow and arrows.

Past studies have examined the environmental conditions and ingredients needed to produce and maintain strong MCSs, as well as bow echoes. That research shows that the cold pool behind the leading line of convection (whether it is linear, or bow shaped)

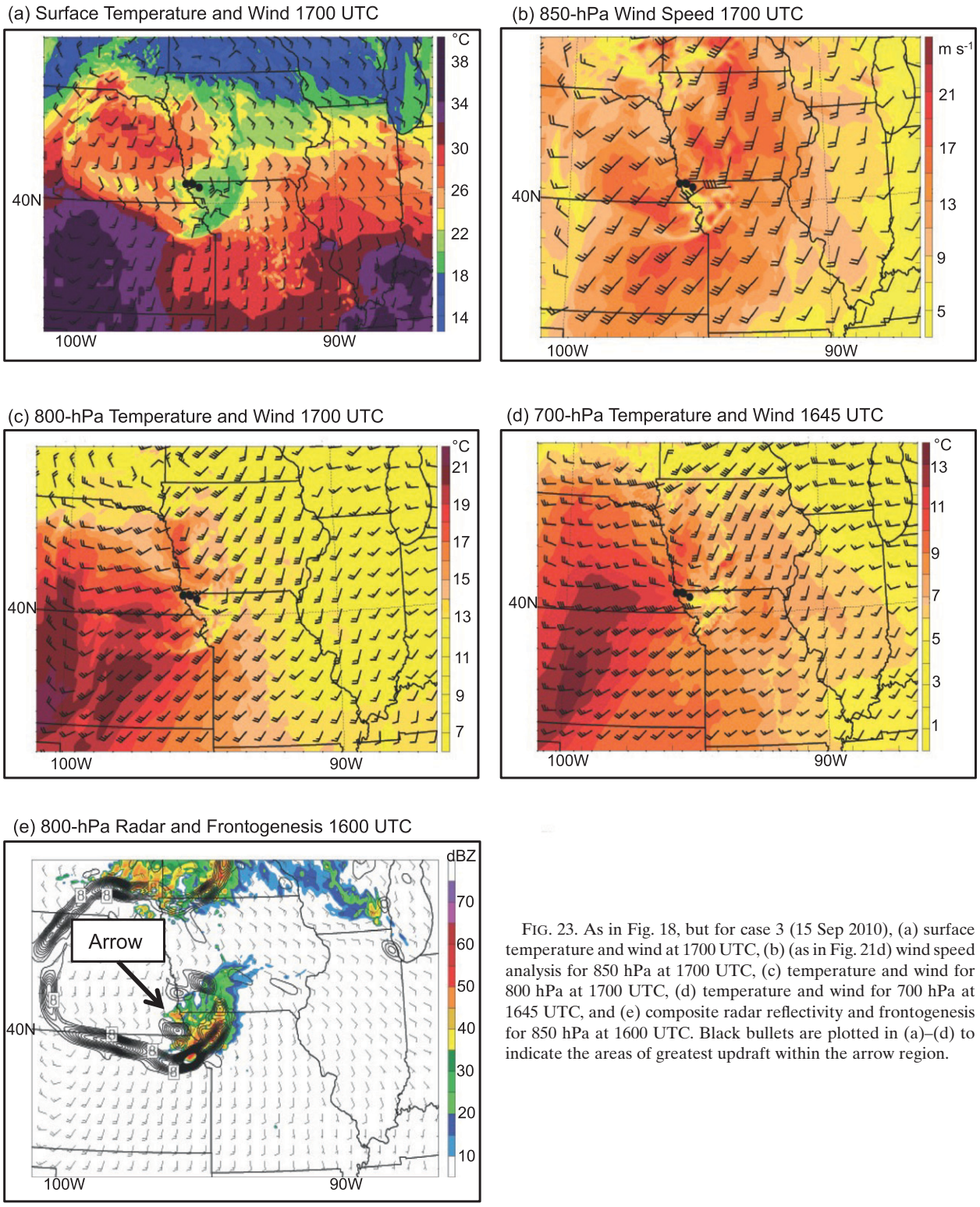

FIG. 23. As in Fig. 18, but for case 3 (15 Sep 2010), (a) surface temperature and wind at 1700 UTC, (b) (as in Fig. 21d) wind speed analysis for 850 hPa at 1700 UTC, (c) temperature and wind for 800 hPa at 1700 UTC, (d) temperature and wind for 700 hPa at 1645 UTC, and (e) composite radar reflectivity and frontogenesis for 850 hPa at 1600 UTC. Black bullets are plotted in (a)–(d) to indicate the areas of greatest updraft within the arrow region.

stabilizes the mesoscale environment, temporarily inhibiting local convection initiation. Studies have shown that the cold pool can serve as a boundary, sometimes inducing secondary convection around its periphery; however, as revealed in the current study, a convective arrow is capable of forming far behind ($L > 100$ km) the cold-pool edge, and sometimes above the top of the cold pool. Additionally, convection within the arrow forms in

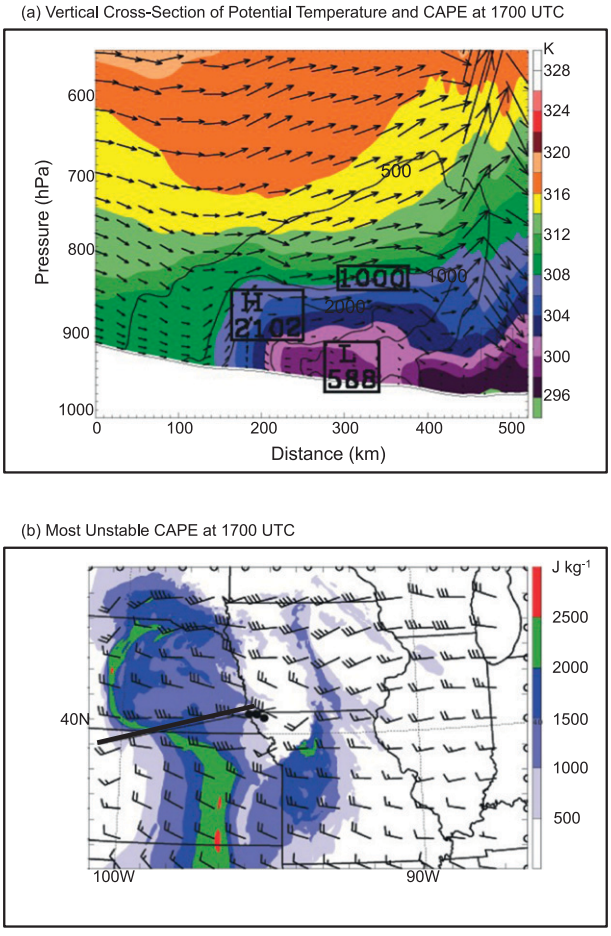

FIG. 24. (a) As in Fig. 19a, but for 1700 UTC 15 Sep 2010, and CAPE is contoured at intervals of 1000 J kg^{-1}. (b) As in Figs. 19b,c, but for 1700 UTC 15 Sep 2010.

an orientation perpendicular to the leading line of convection.

Herein, conventional observations (e.g., surface and radar) and composites from gridded model-based analyses reveal previously found ingredients for major MCSs or bow echoes (e.g., warm advection, sufficient CAPE, and vertical shear), but are insufficiently detailed to elucidate initiation and maintenance mechanisms for the arrow portion of the bow and arrow system. To supplement the observational analysis, convection-permitting numerical simulations are analyzed at much higher spatial and temporal resolution for three selected cases. These simulations seem to replicate the overall reflectivity structure found in observations of the individual cases and reveal several similarities, as well as a few differences, in the environment of the arrow region among the cases.

A schematic diagram (Fig. 25) displays the common environmental features among the cases. The environmental attribute that remains constant for all three cases is southwesterly flow into the arrow region (which is also evident in the observations). This southwesterly flow is associated with an LLJ, which transports warm, moist air into the region above the cold pool, allowing thermodynamic instability to redevelop in the arrow region that had been previously stabilized by the cold pool associated with the bow echo. MUCAPE values are typically maximized upstream (southwest) of the location of arrow formation. However, the warm advection and associated gradual quasi-isentropic ascent contribute to vertical displacements sufficient to allow convection to initiate and be maintained within the arrow region. Although the orientation of convergence differs for each case, it is always evident in the arrow region behind the bow, where the LLJ and northwesterly rear inflow juxtapose. In addition to horizontal convergence, the flow in the region of the arrow has deformation and significant vertical shear along the direction of the arrow (not shown), which may influence the linearity of the convection and its orientation. One of the noted differences among the cases is the source level of air parcels that contribute to convective updrafts in the arrow. Additionally, the orientation of the converging winds (in the arrow region) varies among cases.

In the absence of a full climatology, 14 cases in 12 warm seasons identified using conventional (i.e., operational) data sources does suggest that the coexistence of bow echoes and arrows is relatively unusual; however, given the important consequences of these and related events, it would be beneficial to obtain a larger sample size of events for examination, which would increase the likelihood of more successful simulations. Analyses of additional events would help to confirm representativeness of results found in this study, as well as to provide possible additional explanations for the bow and arrow structure.

Extracting differences in environments from cases that do not create an arrow behind a bow echo is just as important as establishing the features conducive to arrow formation. This was attempted for this study, but was not possible because of a lack of successful simulations. Simulations that were unsuccessful not only failed to create an arrow, but also failed to correctly simulate the prerequisite bow echo. Ideally, using research-grade ensemble forecasts for predictability purposes would create a variety of possible scenarios that would have simulations that create bow and arrows, as well as those that only create the bow echo. Furthermore, idealized simulations initialized with environments representative of those in which bow-and-arrow MCSs form may

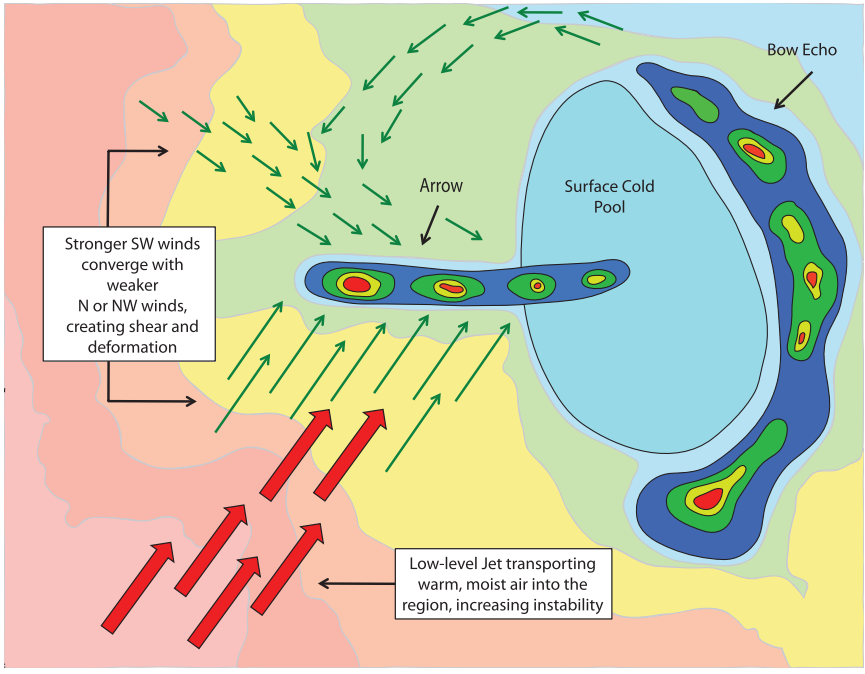

FIG. 25. A schematic diagram showing all the important components of the bow and arrow system. The thick red arrows represent the LLJ, while the thin green arrows represent wind direction and speed (the longer the arrow, the faster the speed) for all pressure levels. The colored contours represent isotherms, where hotter temperatures are in shades of red, and cooling to blue.

provide further insights into the important processes in these events.

Acknowledgments. Morris Weisman (NCAR), Wei Wang (NCAR), and Clark Evans (University of Wisconsin—Milwaukee) are acknowledged for providing forecast data from the National Center for Atmospheric Research, as is NCAR's Bluefire system for their computing resources, and the NCAR Computational and Information Systems Laboratory (CISL) Research Data Archive for providing the input data for simulations. The authors are also grateful to Morris Weisman and Stan Trier (NCAR) for their constructive suggestions that led to improvements and clarifications in the manuscript. This research is supported by the National Science Foundation Grants AGS-0954908 and AGS-1157425. The authors thank Andrea Schumacher for suggesting the ''bow and arrow'' name.

REFERENCES

Augustine, J. A., and F. Caracena, 1994: Lower-tropospheric precursors to nocturnal MCS development over the central United States. *Wea. Forecasting,* **9,** 116–135.

Banacos, P. C., and D. M. Schultz, 2005: The use of moisture flux convergence in forecasting convective initiation: Historical and operational perspectives. *Wea. Forecasting,* **20,** 351–366.

Carbone, R. E., J. D. Tuttle, D. A. Ahijevych, and S. B. Trier, 2002: Inferences of predictability associated with warm season precipitation episodes. *J. Atmos. Sci.,* **59,** 2033–2056.

Chappell, C. F., 1986: Quasi-stationary convective events. *Mesoscale Meteorology and Forecasting,* P. S. Ray, Ed., Amer. Meteor. Soc., 289–310.

Coniglio, M. C., S. F. Corfidi, and J. S. Kain, 2011: Environment and early evolution of the 8 May 2009 derecho-producing convective system. *Mon. Wea. Rev.,* **139,** 1083–1102.

Corfidi, S. F., 2003: Cold pools and MCS propagation: Forecasting the motion of downwind-developing MCSs. *Wea. Forecasting,* **18,** 997–1017.

Doswell, C. A., III, H. E. Brooks, and R. A. Maddox, 1996: Flash flood forecasting: An ingredients-based methodology. *Wea. Forecasting,* **11,** 560–581.

Fujita, T. T., 1955: Results of detailed synoptic studies of squall lines. *Tellus,* **7,** 405–436.

——, 1978: Manual of downburst identification for project NIMROD. Satellite and Mesometeorology Research Paper 156, Department of Geophysical Sciences, University of Chicago, 104 pp.

Glickman, T., Ed., 2000: *Glossary of Meteorology.* 2nd ed. Amer. Meteor. Soc., 855 pp.

Goff, R. C., 1976: Vertical structure of thunderstorm outflows. *Mon. Wea. Rev.,* **104,** 1429–1440.

Hamilton, R. E., 1970: Use of detailed intensity radar data in mesoscale surface analysis of the 4 July 1969 storm in Ohio.

Preprints, *14th Conf. on Radar Meteorology,* Tucson, AZ, Amer. Meteor. Soc., 339–342.

Hong, S., and J. J. Lim, 2006: The WRF single-moment 6-class microphysics scheme (WSM6). *J. Korean Meteor. Soc.,* **42,** 129–151.

——, Y. Noh, and J. Dudhia, 2006: A new vertical diffusion package with an explicit treatment of entrainment processes. *Mon. Wea. Rev.,* **134,** 2318–2341.

Iowa State University, cited 2012: Iowa Environmental Mesonet Warning and Storm Report Archive. [Available online at http://mesonet.agron.iastate.edu/cow.]

Janjic, Z. I., 1994: The step-mountain Eta coordinate model: Further developments of convection, viscous sublayer, and turbulence closure schemes. *Mon. Wea. Rev.,* **122,** 927–945.

Johns, R. H., and C. A. Doswell III, 1992: Severe local storms forecasting. *Wea. Forecasting,* **7,** 588–612.

Johnson, R. H., and P. J. Hamilton, 1988: The relationship of surface pressure features to the precipitation and air flow structure of an intense midlatitude squall line. *Mon. Wea. Rev.,* **116,** 1444–1472.

——, S. L. Aves, P. E. Ciesielski, and T. D. Keenan, 2005: Organization of oceanic convection during the onset of the 1988 East Asian summer monsoon. *Mon. Wea. Rev.,* **133,** 131–148.

Kain, J. S., 2004: The Kain–Fritsch convective parameterization: An update. *J. Appl. Meteor.,* **43,** 170–181.

Klimowski, B. A., M. R. Hjelmfelt, and M. J. Bunkers, 2004: Radar observations of the early evolution of bow echoes. *Wea. Forecasting,* **19,** 727–734.

Koch, S. E., M. DesJardins, and P. J. Kocin, 1983: An interactive Barnes objective map analysis scheme for use with satellite and conventional data. *J. Climate Appl. Meteor.,* **22,** 1487–1503.

LeMone, M. A., E. J. Zipser, and S. B. Trier, 1998: The role of environmental shear and thermodynamic conditions in determining the structure and evolution of mesoscale convective systems during TOGA COARE. *J. Atmos. Sci.,* **55,** 3493–3518.

Lin, Y., and K. E. Mitchell, 2005: The NCEP stage II/IV hourly precipitation analyses: Development and applications. Preprints, *19th Conf. on Hydrology,* San Diego, CA, Amer. Meteor. Soc., 439–451.

Mesinger, F., and Coauthors, 2006: North American Regional Reanalysis. *Bull. Amer. Meteor. Soc.,* **87,** 343–360.

Metz, N. D., and L. F. Bosart, 2010: Derecho and MCS development, evolution, and multiscale interactions during 3–5 July 2003. *Mon. Wea. Rev.,* **138,** 3048–3070.

NOAA, cited 2012a: National Oceanic and Atmospheric Administration Storm Prediction Center product and report archives. [Available online at http: //www.spc.noaa.gov/archive/.]

——, cited 2012b: National Oceanic and Atmospheric Administration Hydrometeorological Prediction Center synoptic scale analysis. [Available online at http://www.hpc.ncep.noaa.gov/html/sfc2.shtml.]

Parker, M. D., and R. H. Johnson, 2000: Organizational modes of midlatitude mesoscale convective systems. *Mon. Wea. Rev.,* **128,** 3413–3436.

Rotunno, R., J. B. Klemp, and M. L. Weisman, 1988: A theory for strong, long-lived squall lines. *J. Atmos. Sci.,* **45,** 463–485.

Schumacher, R. S., and R. H. Johnson, 2005: Organization and environmental properties of extreme-rain-producing mesoscale convective systems. *Mon. Wea. Rev.,* **133,** 961–976.

——, and ——, 2006: Characteristics of U.S. extreme rain events during 1999–2003. *Wea. Forecasting,* **21,** 69–85.

Skamarock, W. C., and J. B. Klemp, 2008: A time-split nonhydrostatic atmospheric model for weather research and forecasting applications. *J. Comput. Phys.,* **227,** 3465–3485.

——, and M. L. Weisman, 2009: The impact of positive-definite moisture transport on NWP precipitation forecasts. *Mon. Wea. Rev.,* **137,** 488–494.

——, and Coauthors, 2008: A description of the Advanced Research WRF version 3. NCAR Tech. Note NCAR/TN-475+STR, 125 pp. [Available online at http://www.mmm.ucar.edu/wrf/users/docs/arw_v3.pdf.]

Thompson, G., P. R. Field, R. M. Rasmussen, and W. D. Hall, 2008: Explicit forecasts of winter precipitation using an improved bulk microphysics scheme. Part II: Implementation of a new snow parameterization. *Mon. Wea. Rev.,* **136,** 5095–5115.

Trier, S. B., C. A. Davis, and D. A. Ahijevych, 2010: Environmental controls on the simulated diurnal cycle of warm-season precipitation in the continental United States. *J. Atmos. Sci.,* **67,** 1066–1090.

Weisman, M. L., 1993: The genesis of severe, long-lived bow echoes. *J. Atmos. Sci.,* **50,** 645–670.

——, and J. B. Klemp, 1986: Characteristics of isolated convective storms. *Mesoscale Meteorology and Forecasting,* P. S. Ray, Ed., Amer. Meteor. Soc., 331–358.

——, and C. A. Davis, 1998: Mechanisms for the generation of mesoscale vortices within quasi-linear convective systems. *J. Atmos. Sci.,* **55,** 2603–2622.

——, J. B. Klemp, and R. Rotunno, 1988: Structure and evolution of numerically simulated squall lines. *J. Atmos. Sci.,* **45,** 1990–2013.

——, C. Davis, W. Wang, K. W. Manning, and J. B. Klemp, 2008: Experiences with 0–36-h explicit convective forecasts with the WRF-ARW model. *Wea. Forecasting,* **23,** 407–437.

Wheatley, D. M., and D. J. Stensrud, 2010: The impact of assimilating surface pressure observations on severe weather events in a WRF mesoscale ensemble system. *Mon. Wea. Rev.,* **138,** 1673–1694.